A 3D hp-adaptive discontinuous Galerkin method for modeling earthquake dynamics

J. Tago,[1] V. M. Cruz-Atienza,[1] J. Virieux,[2] V. Etienne,[3] and F. J. Sánchez-Sesma[4]

Received 15 March 2012; revised 6 August 2012; accepted 14 August 2012; published 26 September 2012.

[1] We introduce a novel scheme, DGCrack, to simulate dynamic rupture of earthquakes in three dimensions based on an hp-adaptive discontinuous Galerkin method. We solve the velocity-stress weak formulation of elastodynamic equations on an unstructured tetrahedral mesh with arbitrary mesh refinements (h-adaptivity) and local approximation orders (p-adaptivity). Our scheme considers second-order fault elements (P2) where dynamic-rupture boundary conditions are enforced through *ad hoc* fluxes across the fault. To model the Coulomb slip-dependent friction law, we introduce a predictor-corrector scheme for estimating shear fault tractions, in addition to a special treatment of the normal tractions that guarantees the continuity of fault normal velocities. We verify the DGCrack by comparison with several methods for two spontaneous rupture tests and find excellent agreement (i.e., rupture times RMS errors smaller than 1.0%) provided that one or more fault elements resolve the fault cohesive zone. For a quantitative comparison, we introduce a methodology based on cross-correlation measurements that provide a simple way to quantify the similarity between solutions. Our verification tests include a 60° dipping normal fault reaching the free surface. The DGCrack method reveals convergence rates close to those of well-established methods and a numerical efficiency significantly higher than that of similar discontinuous Galerkin approaches. We apply the method to the 1992 Landers-earthquake fault system in a layered medium, considering heterogeneous initial stress conditions and mesh adaptivities. Our results show that previously proposed dynamic models for the Landers earthquake require a reevaluation in terms of the initial stress conditions that take account of the intricate fault geometry.

Citation: Tago, J., V. M. Cruz-Atienza, J. Virieux, V. Etienne, and F. J. Sánchez-Sesma (2012), A 3D hp-adaptive discontinuous Galerkin method for modeling earthquake dynamics, *J. Geophys. Res.*, *117*, B09312, doi:10.1029/2012JB009313.

1. Introduction

[2] The availability of high-quality near-field records of large subduction earthquakes in the last few years makes it possible to test and validate physics-based rupture models. The development of sophisticated models to explain such aggregate of observations is now largely justified. Huge efforts have been made by the seismological community in the last ten years to overcome technical limitations preventing most methods for dynamic rupture calculations from integrating the effect of fault geometry in the spontaneous rupture of earthquakes. Because of both its simplicity and efficiency, the finite difference (FD) method has been one of the first and most persistent approaches to simulate rupture dynamics along planar faults [e.g., *Andrews*, 1976; *Madariaga*, 1976; *Miyatake*, 1980; *Day*, 1982; *Virieux and Madariaga*, 1982; *Harris and Day*, 1993; *Madariaga et al.*, 1998; *Peyrat et al.*, 2001; *Day et al.*, 2005; *Dalguer and Day*, 2007]. Although different strategies have been proposed in recent years to integrate complex fault geometries into such methods [*Cruz-Atienza and Virieux*, 2004; *Kase and Day*, 2006; *Cruz-Atienza et al.*, 2007; *Kozdon et al.*, 2012], most common approaches handle numerical lattices (meshes) that are adaptable to the problem geometry (i.e., fault geometry). One set of methods is based on well established boundary integral equations (BIE), [e.g., *Das and Aki*, 1977; *Andrews*, 1985; *Cochard and Madariaga*, 1994; *Kame and Yamashita*, 1999; *Aochi et al.*, 2000; *Lapusta et al.*, 2000; *Hok and Fukuyama*, 2011]. However, since these methods discretize only boundaries and require semi-analytical approximations of Green functions, they have difficulties integrating heterogeneities of the bulk properties into which the fault is embedded. The other set consists of domain methods based on weak formulations of the

[1]Instituto de Geofísica, Universidad Nacional Autónoma de México, Mexico City, Mexico.
[2]Institut des Sciences de la Terre, Université Joseph Fourier, Grenoble, France.
[3]Géoazur, Univeristé de Nice-Sophia Antipolis, Nice, France.
[4]Instituto de Ingeniería, Universidad Nacional Autónoma de México, Mexico City, Mexico.

Corresponding author: J. Tago, Instituto de Geofísica, Universidad Nacional Autónoma de México, 04510 Mexico City, Distrito Federal, Mexico. (josue.tago@gmail.com)

0148-0227/12/2012JB009313

elastodynamic equations, and can be separated into two subgroups depending on how the lattice boundaries are treated. On one hand the continuous finite element methods (FEM), whose formulations require continuity between the mesh elements except where special treatments of boundary conditions are imposed [e.g., *Oglesby and Day*, 2001; *Ampuero*, 2002; *Festa and Vilotte*, 2006; *Ma and Archuleta*, 2006; *Kaneko et al.*, 2008; *Ely et al.*, 2009; *Barall*, 2009]. On the other, the discontinuous finite element methods, better known as the discontinuous Galerkin (DG) methods, which only consider fluxes between elements and, therefore, do not impose any field continuity across their boundaries.

[3] When studying the earthquakes source physics, the discontinuity produced across the fault by the rupture process must be accurately treated, so that the DG strategy is naturally suitable for tackling this problem.

[4] The first dynamic rupture model based on a DG approach was introduced in two dimensions (2D) by *Benjemaa et al.* [2007] for low-order (P0) interpolation functions. In this case, where the basis functions are constants, the DG schemes are also known as finite volume (FV) methods [*LeVeque*, 2002] and provide computationally efficient algorithms that are as fast as second order FD schemes (i.e., they are equivalent in efficiency on rectangular meshes). However, the extension to three dimensions (3D) of this model [*Benjemaa et al.*, 2009] revealed convergence problems for unstructured tetrahedral grids (e.g., non-planar faults) [*Tago et al.*, 2010]. On these irregular grids, P0 elements have zero-order convergence for wave propagation modeling due to the centered flux approximation [*Brossier et al.*, 2009; *Remaki et al.*, 2011], so increasing the element interpolation order to achieve a proper numerical convergence of wave propagation with a DG scheme is mandatory. Nevertheless, in practice, high-order convergence rates are not clearly observed for the dynamic-rupture numerical problem (i.e., 4th order or higher), and second order interpolation methods are often the most accurate and efficient approximations for applying the corresponding fault boundary conditions [*Cruz-Atienza et al.*, 2007; *Moczo et al.*, 2007; *Rojas et al.*, 2009; *Kozdon et al.*, 2012]. A notable case for which the convergence rate is essentially insensitive to increments in the interpolation order is the ADER-DG discontinuous Galerkin method for 2D and 3D geometries by *de la Puente et al.* [2009] and *Pelties et al.* [2012], respectively, despite its spectral convergence for the wave propagation problem [*Dumbser and Käser*, 2006]. The ADER-DG is based on a modal interpolation formulation, instead of the nodal interpolation we consider here. Both formulations are mathematically equivalent but computationally different [*Hesthaven and Warburton*, 2008]. Our choice of using the nodal approximation essentially relies on the fact that the evaluation of fluxes requires fewer computations than in a modal scheme, as we shall explain on section 4.1.

[5] In this work we introduce a novel discontinuous Galerkin approach, namely the DGCrack method, to model the dynamic rupture of earthquakes in 3D geometries. The numerical platform of our model is the GeoDG3D parallel code [*Etienne et al.*, 2010] developed for the elastic wave propagation. For the parallel implementation it uses the Message Passing Interface (MPI) and achieves ~80% strong scalability. GeoDG3D accounts for free surface boundary conditions along arbitrary topographies, and includes Convolutional Perfectly Matching Layer (CPML) absorbing boundary conditions at the external edges of the physical domain [*Etienne et al.*, 2010, and references therein]. Furthermore, intrinsic attenuation has been recently introduced into GeoDG3D via the rock quality Q [*Tago et al.*, 2010], but will not be discussed in the present work. To maximize both the efficiency and the accuracy of the scheme depending on the model properties and geometry, the method handles unstructured mesh refinements (i.e., h-adaptivity) and locally adapts the order of the nodal interpolations (i.e., within every grid element; p-adaptivity) [*Etienne et al.*, 2010].

[6] We first introduce the mathematical and computational concepts for the 3D dynamic rupture problem, and then assess both its accuracy and convergence rate by comparing calculated solutions with those yielded by finite difference (DFM), finite element (FEM), spectral boundary integral (MDSBI) and spectral element (SPECFEM3D) methods for two spontaneous rupture benchmark tests [*Harris et al.*, 2009]. Since one of our major goals in the near future is the investigation of dynamic rupture propagation along realistic (nonplanar) fault geometries, we take special care to verify the accuracy of the normal stress field across the fault during rupture propagation, as the fault normal tractions strongly determine the radiated energy throughout the Coulomb failure criterion. We finally illustrate the capabilities of the DGCrack method through a spontaneous rupture simulation along the 1992 Landers earthquake fault system, which is a geometrically intricate and physically interesting study case.

2. Elastodynamic Equations

[7] Velocities and stresses induced by the propagation of waves in a homogeneous elastic medium can be modeled with a first order hyperbolic system [*Madariaga*, 1976]. Following the transformation proposed by *Benjemaa et al.* [2009], a pseudo-conservative form of the system is given by

$$\begin{aligned} \rho\partial_t\vec{v} &= \sum_{\theta\in\{x,y,z\}} \partial_\theta(\mathcal{M}_\theta\vec{\sigma}) \\ \Lambda\partial_t\vec{\sigma} &= \sum_{\theta\in\{x,y,z\}} \partial_\theta(\mathcal{N}_\theta\vec{v}), \end{aligned} \tag{1}$$

where $\vec{v} = \left(v_x, v_y, v_z\right)^T$ is the velocity vector and $\vec{\sigma} = \left(\omega, \omega', \omega'', \sigma_{xy}, \sigma_{xz}, \sigma_{yz}\right)^T$. To avoid physical properties on the right hand side of (1), a change of variables is applied to the stress vector leading to its first three components

$$\begin{aligned} \omega &= \frac{1}{3}\left(\sigma_{xx} + \sigma_{yy} + \sigma_{zz}\right) \\ \omega' &= \frac{1}{3}\left(2\sigma_{xx} - \sigma_{yy} - \sigma_{zz}\right) \\ \omega'' &= \frac{1}{3}\left(-\sigma_{xx} + 2\sigma_{yy} - \sigma_{zz}\right), \end{aligned} \tag{2}$$

which involve the mean and the deviatoric stresses.

[8] In this model, the physical properties of the medium are the density, ρ, and the medium matrix $\Lambda = \mathrm{diag}(3/(3\lambda + 2G), 3/(2G), 3/(2G), 1/G, 1/G, 1/G)$ which is composed of the Lamé parameters λ and G. The terms $\mathcal{M}_\theta$ and $\mathcal{N}_\theta$ are constant real matrices whose definition can be seen in Appendix B.

2.1. The hp-Adaptive Discontinuous Galerkin Scheme

[9] To construct the local approximation of the hyperbolic system (1), we first decompose the domain Ω into K elements, such that

$$\Omega \simeq \Omega_h = \sum_{i=1}^{K} D_i, \tag{3}$$

where each D_i is a straight-sided tetrahedron and the mesh (i.e., decomposed domain) is assumed to be geometrically conforming. By applying a Discontinuous Galerkin approach to the weak formulation of (1) as proposed by *Etienne et al.* [2010], we obtain the following velocity-stress iterative scheme in every i-tetrahedron,

$$\rho_i(\mathcal{I}_3 \otimes \mathcal{K}_i)\frac{\vec{v}_i^{n+\frac{1}{2}} - \vec{v}_i^{n-\frac{1}{2}}}{\Delta t} = -\sum_{\theta\in\{x,y,z\}} (\mathcal{M}_\theta \otimes \mathcal{E}_{i\theta})\vec{\sigma}_i^n + \frac{1}{2}\sum_{k\in N_i}\left[(\mathcal{P}_{ik}\otimes\mathcal{F}_{ik})\vec{\sigma}_i^n + (\mathcal{P}_{ik}\otimes\mathcal{G}_{ik})\vec{\sigma}_k^n\right] \tag{4}$$

$$(\Lambda_i \otimes \mathcal{K}_i)\frac{\vec{\sigma}_i^{n+1} - \vec{\sigma}_i^n}{\Delta t} = -\sum_{\theta\in\{x,y,z\}} (\mathcal{N}_\theta \otimes \mathcal{E}_{i\theta})\vec{v}_i^{n+\frac{1}{2}} + \frac{1}{2}\sum_{k\in N_i}\left[(\mathcal{Q}_{ik}\otimes\mathcal{F}_{ik})\vec{v}_i^{n+\frac{1}{2}} + (\mathcal{Q}_{ik}\otimes\mathcal{G}_{ik})\vec{v}_k^{n+\frac{1}{2}}\right], \tag{5}$$

where the superscript n indicates the time step, N_i is the group of adjacent elements to the i-tetrahedron and $\otimes$ represents the tensor product. The matrices involved are the mass matrix, $\mathcal{K}_i$, the stiffness matrices, $\mathcal{E}_{i\theta}$, for all $\theta \in \{x, y, z\}$, the flux matrices, $\mathcal{F}_{ik}$ and $\mathcal{G}_{ik}$, and the auxiliary flux matrices, $\mathcal{Q}_{ik}$ and $\mathcal{P}_{ik}$. A derivation of the numerical scheme and the matrices definition can be found in Appendix A. The size of these matrices depends on the order of the polynomial basis (e.g., P0, P1, P2, …, Pk) used for the nodal interpolation. Staggered time integration is done through a second-order explicit leap-frog scheme, which allows the alternation of velocities and stresses computation.

[10] One of the main features of this scheme is the h-adaptivity, which allows working with unstructured tetrahedral meshes and thus to adapt the mesh geometry to both the physical properties of the medium and the problem geometry (i.e., mesh refinement). Furthermore, the p-adaptivity is possible thanks to the fluxes between neighboring elements, which are such that two adjacent tetrahedra may have different interpolation orders. The fluxes are computed via a non-dissipative centered scheme that allows choosing different degrees of freedom (DOF) in every tetrahedron. As shown by *Etienne et al.* [2010], the p-adaptivity is a powerful tool for the optimization of the domain discretization by adapting the element order to the medium waves speed. Our scheme includes finite volume approximation orders, P0 (i.e., constant functions), linear interpolation functions, P1, and quadratic interpolation functions, P2. *Etienne et al.* [2010] have shown that this scheme is efficient and accurate enough for modeling wave propagation in large domains and in highly heterogeneous elastic media. The accuracy for P2 elements with unstructured tetrahedral meshes is achieved with 3 tetrahedra per minimum wavelength, which is comparable with the 5 grid points required by the fourth-order staggered-grid finite difference method [*Levander*, 1988], while the stability is determined with an heuristic criterion proposed by *Käser and Dumbser* [2008] expressed as

$$\Delta t < \min_i \left(\frac{1}{2k_i + 1} * \frac{2r_i}{v_{p_i}}\right),$$

where r_i is the radius of the sphere inscribed in the element indexed by i, v_{p_i} is the P-wave velocity in the element and k_i is the polynomial degree used in the element.

[11] The distribution of interpolation orders in the computational domain is such that P0 elements describe the CPML slab while elements with both P1 and P2 approximations discretize the physical domain depending on their sizes. This enhances the accuracy of the scheme and minimizes the computational load. Current computational developments will allow us in the near future to consider higher interpolation orders away from the rupture zone for large-distance wave propagation.

3. Dynamic Rupture Model

[12] Earthquakes are highly nonlinear phenomena produced by sliding instabilities along geological faults. The stability of the rupture system depends on several physical factors, like the initial state of stresses in the earth, the material properties and rheology, the sliding rate, the fault geometry, and the constitutive relationship governing the mechanics of the rupture surface. During rupture propagation, fault tractions evolve dynamically depending on all these factors, and the accuracy of an earthquake model strongly depends on the correctness of boundary conditions applied to these tractions in accordance with the fault constitutive relationship (i.e., friction law), which in turn depends on the accurate energy transportation through elastic waves in the medium. Insuring the accuracy of both boundary conditions (local feature) and wave propagation (global feature) has long been a difficult task for many seismologists. In the next sections, we shall introduce both the fault boundary conditions and the friction law used in our dynamic source model and then its formulation into the DG scheme. In spite of the attention they deserve, we will not discuss the features of wave propagation in this study since they have been previously analyzed by *Etienne et al.* [2010] and *Tago et al.* [2010].

3.1. Boundary Conditions and Friction Law

[13] The fault, Γ, is a piecewise discretized surface with a directed normal vector $\vec{n}$, such that each side of each surface element is clearly identified. Slip and stresses over Γ are related through a friction law in such a way that the fault tangential tractions evolve according to that law, which in turn depends, for instance, on some fault kinematic parameter (i.e., slip and slip rate) and wave propagation in the surroundings of the rupture tip. On the other hand, the strain field is accommodated, in the elastic medium, through displacement (i.e., velocity) discontinuities across Γ. It is thus convenient to split our domain into a plus- and a minus-side

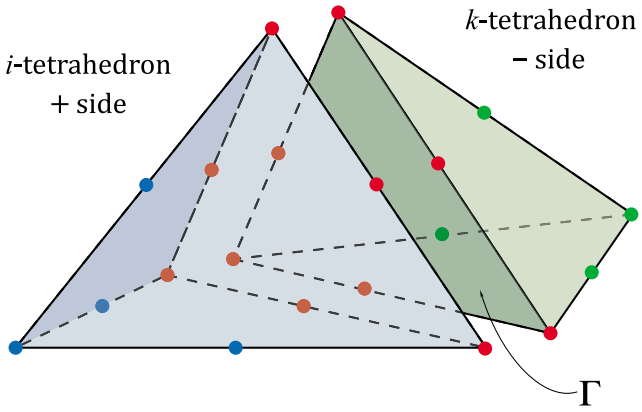

Figure 1. Second-order (P2) interpolation-order tetrahedra illustrating two mesh elements shearing the fault surface Γ. Red dots represent the six split nodes (i.e., two collocated nodes, one per element) lying on the fault from which the fluxes across Γ are computed and the dynamic-rupture boundary conditions applied.

with respect to the fault (Figure 1) and express the limiting velocity field, $\vec{v}$, over Γ as

$$\vec{v}^{\pm}(t,\vec{x}) = \lim_{\epsilon \to 0} \vec{v}(t,\vec{x} \pm \epsilon \vec{n}(\vec{x})) \qquad \epsilon \in \mathbb{R}.$$

[14] Furthermore, we define the normal and tangential components of $\vec{v}^{\pm}$ with respect to $\vec{n}$ as

$$\vec{v}_N^{\pm} = (\vec{n}\cdot\vec{v}^{\pm})\vec{n}$$
$$\vec{v}_T^{\pm} = \vec{v}^{\pm} - \vec{v}_N^{\pm} = \vec{v}^{\pm} - (\vec{n}\cdot\vec{v}^{\pm})\vec{n}.$$

[15] Now we can define the vector $\vec{V}$ as the velocity discontinuity across Γ, where its fault tangential component, namely the fault slip rate, is

$$\vec{V}_T := [[\vec{v}_T]] = \vec{v}_T^{+} - \vec{v}_T^{-}, \tag{6}$$

and its fault normal component is

$$\vec{V}_N := [[\vec{v}_N]] = \vec{v}_N^{+} - \vec{v}_N^{-}. \tag{7}$$

[16] The slip magnitude at any time t is thus defined as the integral of the modulus of $\vec{V}_T$ over time given by

$$U(t) = \int_0^t \left\| \vec{V}_T(s,\vec{x}) \right\| ds. \tag{8}$$

[17] The dynamic rupture boundary conditions on the fault are the following two jump conditions, involving the tangential fields [*Day et al.*, 2005],

$$\tau_c - \left\| \vec{T}_T \right\| \geq 0 \tag{9}$$

$$\tau_c \vec{V}_T - \vec{T}_T \left\| \vec{V}_T \right\| = 0, \tag{10}$$

and a third jump condition applied to (7)

$$\vec{V}_N = 0, \tag{11}$$

where $\vec{T}_T$ is the fault tangential traction vector and τ_c is the fault frictional strength. The fault strength is determined by the Coulomb friction law, which depends on the fault normal stress (with negative values for compression), σ_N, the friction coefficient, μ, and the fault cohesion, C, as

$$\tau_c = C - \sigma_N \mu. \tag{12}$$

[18] Condition (9) provides an upper bound to the magnitude of $\vec{T}_T$ to the fault strength, τ_c, that always acts opposite to sliding on Γ. The second condition (10) forces the slip rate to be parallel to $\vec{T}_T$, the tangential traction. Another implication of these jump conditions is that, whenever the inequality of (9) holds, the slip rate vector is zero, which can be easily seen through the modulus of (10). Finally, condition (11) implies that there is neither fault opening nor mass interpenetration across the fault during rupture propagation.

[19] In nature, the friction coefficient depends on the fault slip, slip rate and state variables accounting for the sliding history and fault age [e.g., *Dieterich*, 1979; *Ruina*, 1983]. However, we shall assume a simple slip weakening law [*Ida*, 1972; *Palmer and Rice*, 1973], which makes μ linearly depend on the slip as

$$\mu(U) = \mu_0 + (\mu_s - \mu_d)\left(1 - \frac{U}{\delta_0}\right) H\left(1 - \frac{U}{\delta_0}\right), \tag{13}$$

where $H(\cdot)$ is the Heaviside function, μ_s and μ_d are the static and dynamic friction coefficients, respectively, and δ_0 is the critical slip weakening distance.

[20] A series of studies have tried to estimate δ_0 from historical earthquakes based on indirect source observations through the inversion of strong motion seismograms [e.g., *Ide and Takeo*, 1997; *Mikumo and Yagi*, 2003]. However, due to the limited bandwidth of the seismograms, the slip weakening distance was poorly resolved in these studies. Moreover, dynamic models based on such indirectly inferred δ_0 values may be biased and not able to resolve the stress breakdown process over the fault [*Guatteri and Spudich*, 2000; *Spudich and Guatteri*, 2004]. Direct observation of δ_0 from near-field data is seldom possible [*Cruz-Atienza et al.*, 2009]; except for some isolated cases where rupture propagated with supershear speeds [*Cruz-Atienza and Olsen*, 2010].

[21] The manner by which we incorporate the fault model given by both the jump conditions (9) to (11), and the friction law (12) and (13), into our DG scheme is presented next.

3.2. Discrete Source Model

[22] The domain decomposition introduced in equation (3) should account for the presence of Γ, such that the fault surface is discretized by triangles lying on the faces of adjacent tetrahedra (Figure 1); that is, we preclude Γ to be embedded inside any tetrahedron D_i. The physical domain, Ω, is then decomposed as follows

$$\Omega \simeq \Omega_h = \sum_{i=1}^{K} D_i \text{ such that if } \Gamma \subset \Omega \text{ then } \{\forall D_i : (D_i \backslash S_i) \cap \Gamma = \emptyset\},$$

where each D_i is a straight-sided tetrahedron with surface S_i and the union of all K elements describes a geometrically conforming mesh. The order of the polynomial basis chosen in our method corresponds to P2 quadratic functions because higher approximation orders do not significantly improve neither the accuracy of the dynamic-rupture numerical schemes nor their convergence rate [e.g., *Moczo et al.*, 2007; *Rojas et al.*, 2009; *Pelties et al.*, 2012]. As we shall see, keeping a low approximation order (i.e., P2 interpolation functions) provides both good accuracy and efficiency to our numerical scheme.

[23] Since every tetrahedron has its own nodes in the nodal form of the DG method (i.e., ten independent nodes for P2 elements, Figure 1), a fault node is then composed of two co-located nodes (i.e., a split-node). One of them belongs to the *i*-tetrahedron within the plus-side of the domain and the other to the adjacent *k*-tetrahedron in the minus-side (see Figure 1). This means that each split-node lies between two tetrahedra sharing a fault element. Furthermore, since the DG method does not require field continuity over the element faces, the dislocation produced by the rupture may be handled naturally over the fault, Γ, through the discontinuity of the tangential velocities $\vec{v}_T^{\pm} = \{\vec{v}_{i_T}, \vec{v}_{k_T}\}$. However, this should be treated carefully because most of the elastic fields must remain continuous across Γ.

[24] System (4) and (5) is solved everywhere inside Ω except over Γ, where jump conditions (9) to (11) must be verified. However, as pointed out by *Benjemaa et al.* [2009], before treating the fault fluxes accordingly we should notice that the system is not symmetric because of

$$\mathcal{Q}_{ik} \neq (\mathcal{P}_{ik})^T,$$

which is due to the variable transformation (2) required to group all the medium properties on the left-hand side. Although our method does not require the system to be symmetric, that condition is convenient because then our scheme for P0 elements essentially reduces to the one proposed by *Benjemaa et al.* [2009] (i.e., finite volume approach), which was derived from energy balance consideration across the fault.

[25] To obtain a symmetric system, we first multiply (5) by the symmetrical positive definite matrix $\mathcal{S}$, defined in Appendix B, and then we isolate the updated field values to get the equivalent symmetric system

$$\vec{v}_i^{n+\frac{1}{2}} = \vec{v}_i^{n-\frac{1}{2}} + \frac{\Delta t}{\rho_i}(\mathcal{I}_3 \otimes \mathcal{K}_i)^{-1}\left[-\sum_{\theta\in\{x,y,z\}}(\mathcal{M}_\theta \otimes \mathcal{E}_{i\theta})\vec{\sigma}_i^n + \frac{1}{2}\sum_{k\in N_i}\left[(\mathcal{P}_{ik}\otimes\mathcal{F}_{ik})\vec{\sigma}_i^n + (\mathcal{P}_{ik}\otimes\mathcal{G}_{ik})\vec{\sigma}_k^n\right]\right] \tag{14}$$

$$\vec{\sigma}_i^{n+1} = \vec{\sigma}_i^n + \Delta t\left(\Lambda_i^S \otimes \mathcal{K}_i\right)^{-1}\left[-\sum_{\theta\in\{x,y,z\}}\left(\mathcal{N}_\theta^S \otimes \mathcal{E}_{i\theta}\right)\vec{v}_i^{n+\frac{1}{2}} + \frac{1}{2}\sum_{k\in N_i}\left[\left(\mathcal{P}_{ik}^T\otimes\mathcal{F}_{ik}\right)\vec{v}_i^{n+\frac{1}{2}} + \left(\mathcal{P}_{ik}^T\otimes\mathcal{G}_{ik}\right)\vec{v}_k^{n+\frac{1}{2}}\right]\right], \tag{15}$$

where $\Lambda_i^S = \mathcal{S}\Lambda_i$, $\mathcal{N}_\theta^S = \mathcal{S}\mathcal{N}_\theta$ and $\mathcal{P}_{ik}^T = \mathcal{S}\mathcal{Q}_{ik}$.

[26] Since the fluxes across the fault elements $S_{i\Gamma} = \{S_{ik} \subseteq \Gamma | S_{ik} := S_i \cap S_k\}$ must satisfy the jump conditions (9) to (11), we cannot simply use the centered scheme proposed by *Etienne et al.* [2010] for fluxes between regular elements. Introducing the fault vector fluxes $\vec{f}_i$ and $\vec{g}_i$ for the velocity and stress schemes, respectively, the system (14) and (15) may be rewritten as

$$\vec{v}_i^{n+\frac{1}{2}} = \vec{v}_i^{n-\frac{1}{2}} + \frac{\Delta t}{\rho_i}(\mathcal{I}_3 \otimes \mathcal{K}_i)^{-1}\left[-\sum_{\theta\in\{x,y,z\}}(\mathcal{M}_\theta \otimes \mathcal{E}_{i\theta})\vec{\sigma}_i^n + \frac{1}{2}\sum_{\substack{k\in N_i \\ S_{ik}\cap\Gamma=\emptyset}}\left[(\mathcal{P}_{ik}\otimes\mathcal{F}_{ik})\vec{\sigma}_i^n + (\mathcal{P}_{ik}\otimes\mathcal{G}_{ik})\vec{\sigma}_k^n\right] + \delta_\Gamma(\mathcal{I}_3\otimes\mathcal{G}_{ik})\vec{f}_i^n\right] \tag{16}$$

$$\vec{\sigma}_i^{n+1} = \vec{\sigma}_i^n + \Delta t\left(\Lambda_i^S \otimes \mathcal{K}_i\right)^{-1}\left[-\sum_{\theta\in\{x,y,z\}}\left(\mathcal{N}_\theta^S \otimes \mathcal{E}_{i\theta}\right)\vec{v}_i^{n+\frac{1}{2}} + \frac{1}{2}\sum_{\substack{k\in N_i \\ S_{ik}\cap\Gamma=\emptyset}}\left[\left(\mathcal{P}_{ik}^T\otimes\mathcal{F}_{ik}\right)\vec{v}_i^{n+\frac{1}{2}} + \left(\mathcal{P}_{ik}^T\otimes\mathcal{G}_{ik}\right)\vec{v}_k^{n+\frac{1}{2}}\right] + \delta_\Gamma(\mathcal{I}_3\otimes\mathcal{G}_{ik})\vec{g}_i^{n+\frac{1}{2}}\right], \tag{17}$$

where δ_Γ is a Kronecker delta that is 1 if $S_{i\Gamma} \neq \emptyset$ and 0 otherwise.

[27] Since the fault boundary conditions (9) to (11) must be applied to the traction vector $\vec{T}$, following *Benjemaa et al.* [2009] we notice that the flux in the velocity scheme (14) through any element surface may be expressed in terms of tractions as

$$\frac{1}{2}\left[(\mathcal{P}_{ik}\otimes\mathcal{F}_{ik})\vec{\sigma}_i^n + (\mathcal{P}_{ik}\otimes\mathcal{G}_{ik})\vec{\sigma}_k^n\right] = \frac{1}{2}\left[(\mathcal{I}_3\otimes\mathcal{F}_{ik})\vec{T}_i^n + (\mathcal{I}_3\otimes\mathcal{G}_{ik})\vec{T}_k^n\right].$$

[28] By imposing continuity of $\vec{T}_i$ over the fault element $S_{i\Gamma}$ (i.e., $\vec{T}_{ik}^n = T_i^n = T_k^n$) and assuming the same approximation

order in the two tetrahedra sharing the element (i.e., $\mathcal{F}_{ik} = \mathcal{G}_{ik}$), we set the flux vector across the fault, $\vec{f}_i^n$, to the unique traction vector $\vec{T}_{ik}^n$, and define the flux across the fault as

$$(\mathcal{I}_3 \otimes \mathcal{G}_{ik})\vec{f}_i^n = (\mathcal{I}_3 \otimes \mathcal{F}_{ik})\vec{T}_{ik}^n. \tag{18}$$

[29] By substituting (18) into the velocity scheme (16) and regrouping the terms excluding the flux across the fault on $\vec{R}_i^n$, we obtain

$$\vec{v}_i^{n+\frac{1}{2}} = \vec{v}_i^{n-\frac{1}{2}} + \vec{R}_i^n + \delta_\Gamma \frac{\Delta t}{\rho_i}(\mathcal{I}_3 \otimes \mathcal{K}_i)^{-1}(\mathcal{I}_3 \otimes \mathcal{F}_{ik})\vec{T}_{ik}^n, \tag{19}$$

where

$$\vec{R}_i^n = \frac{\Delta t}{\rho_i}(\mathcal{I}_3 \otimes \mathcal{K}_i)^{-1}\left[- \sum_{\theta\in\{x,y,z\}} (\mathcal{M}_\theta \otimes \mathcal{E}_{i\theta})\vec{\sigma}_i^n + \frac{1}{2} \sum_{\substack{k\in N_i \\ S_{ik}\cap\Gamma=\emptyset}} \left[(\mathcal{P}_{ik} \otimes \mathcal{F}_{ik})\vec{\sigma}_i^n + (\mathcal{P}_{ik} \otimes \mathcal{G}_{ik})\vec{\sigma}_k^n\right]\right].$$

Because the fault normal stress determines the frictional strength via (12), and because boundary conditions are applied to the shear tractions, the fault traction vector $\vec{T}_{ik}^n$ has to be decomposed into its tangential, $\vec{T}_{ik_T}^n$, and normal, $\vec{T}_{ik_N}^n$, components to rewrite the velocity scheme (19) as

$$\vec{v}_i^{n+\frac{1}{2}} = \vec{v}_i^{n-\frac{1}{2}} + \vec{R}_i^n + \delta_\Gamma \frac{\Delta t}{\rho_i}(\mathcal{I}_3 \otimes \mathcal{K}_i)^{-1}(\mathcal{I}_3 \otimes \mathcal{F}_{ik})\left(\vec{T}_{ik_T}^n + \vec{T}_{ik_N}^n\right). \tag{20}$$

3.2.1. Fluxes Across the Fault for the Velocity Scheme (20)

[30] For updating velocities on Γ, we need to specify the flux across the fault in (20). For this we require $\vec{T}_{ik_T}^n$ such that the jump conditions (9) and (10) are fulfilled, and $\vec{T}_{ik_N}^n$ such that the continuity of the fault normal velocity is also guaranteed (condition (11)). All traction conditions must be verified at every fault node and for every time step.

[31] Let us assume that $S_{i\Gamma} \neq \emptyset$ so $\delta_\Gamma = 1$ in (20), where the i- and k-tetrahedra lie at the plus-side and the minus-side of the fault Γ, respectively. Then we define $\vec{V}_{ik}$ to be the velocity discontinuity between the i- and k-tetrahedra over the face Γ. To compute the fault tangential tractions, $\vec{T}_{ik_T}^n$, we first notice that the inequality of condition (9) along with the modulus of (10) implies that

$$\vec{V}_{ik_T} = 0, \tag{21}$$

which means that, whenever $\left\|\vec{T}_{ik_T}^n\right\|$ remains below the frictional strength, τ_c, the tangential traction must ensure the continuity of the tangential velocities at every fault node shared by the i- and k-tetrahedral.

[32] Since we only deal with fault nodes, we thus construct the matrix $\mathcal{K}_{i_\Gamma}^{-1}$, which is the inverse mass matrix whose components depend exclusively on those nodes. It is simply constructed from $\mathcal{K}_i^{-1}$ by eliminating its rows and columns associated with the off-fault nodes.

[33] The computation of $\vec{T}_{ik_T}^n$ verifying condition (21) requires both tetrahedra sharing a fault element to have the same order, so that the nodes in both sides of the fault match to each other (see Figure 1). Besides this, for the specific contribution of $\vec{T}_{ik_T}^n$, we need to compute the volume and surface integrals of $\mathcal{K}_{i_\Gamma}^{-1}$ and $\mathcal{F}_{ik}$, respectively, in a standard element [*Zienkiewicz et al.*, 2005] such that

$$\mathcal{K}_{i_\Gamma}^{-1} = \frac{1}{V_i}\mathcal{K}_{e_\Gamma}^{-1} \text{ and } \mathcal{F}_{ik} = S_{ik}\mathcal{F}_e, \tag{22}$$

where V_i, the i-tetrahedron volume, and S_{ik}, the i-tetrahedron fault surface, are the corresponding Jacobians. Then by substituting (19) into definition (6) and using (22), we express the slip rate vector as

$$\vec{V}_{ik_T}^{n+\frac{1}{2}} := \vec{v}_{i_T}^{n+\frac{1}{2}} - \vec{v}_{k_T}^{n+\frac{1}{2}} = \vec{V}_{ik_T}^{n-\frac{1}{2}} + \vec{R}_{i_T}^n - \vec{R}_{k_T}^n + \Delta t S_{ik}\left(\frac{1}{\rho_i V_i} + \frac{1}{\rho_k V_k}\right) \cdot (\mathcal{I}_3 \otimes \mathcal{K}_{e_\Gamma})^{-1}(\mathcal{I}_3 \otimes \mathcal{F}_e)\mathcal{T}_{ik_T}^n. \tag{23}$$

For computing the tangential traction, we use (21) into (23), which leaves us the following expression

$$\vec{T}_{ik_T}^n = \left(\frac{\rho_i\rho_k V_i V_k}{\Delta t S_{ik}(\rho_i V_i + \rho_k V_k)}\right)(\mathcal{I}_3 \otimes \mathcal{F}_e)^{-1}(\mathcal{I}_3 \otimes \mathcal{K}_{e_\Gamma}) \cdot \left(-\vec{V}_{ik_T}^{n-\frac{1}{2}} - \vec{R}_{i_T}^n + \vec{R}_{k_T}^n\right). \tag{24}$$

[34] This procedure ensures the continuity of the tangential velocity across the fault. However, if the time-dependent frictional strength, τ_c^n, is overcome by the modulus of the tangential traction, $\left\|\vec{T}_{ik_T}^n\right\|$, rupture must occur and the tangential velocity is no longer continuous across the associated fault node. In that case, the equality of condition (9) holds so that

$$\tau_c^n - \left\|\vec{T}_{ik_T}^n\right\| = 0 \Leftrightarrow \left\|\vec{T}_{ik_T}^n\right\| = \tau_c^n.$$

[35] Therefore, to compute the slip rate (23) at every fault node and for every time step, the tangential traction is adjusted according to the following criterion, which depends on whether or not the fault point has broken:

$$\vec{T}_{ik_T}^n = \begin{cases} \vec{T}_{ik_T}^n & \text{if } \left\|\vec{T}_{ik_T}^n\right\| < \tau_c^n, \\ \dfrac{\vec{T}_{ik_T}^n}{\left\|\vec{T}_{ik_T}^n\right\|}\tau_c & \text{if } \left\|\vec{T}_{ik_T}^n\right\| \geq \tau_c^n. \end{cases} \tag{25}$$

[36] Since the nodes within a fault element are coupled through the flux matrix, $\mathcal{F}_{ik}$, and the mass matrix, $\mathcal{K}_{i_\Gamma}$, when

rupture happens in a given node and the condition (25) is imposed, tractions in the remaining nodes change for the same time step. Thus, to accurately and simultaneously satisfy (25) on every fault node, i.e., to allow rupture propagation inside the fault elements, we use an iterative *predictor-corrector* (PC) scheme. If n_{fault} is the number of nodes in a given fault element (i.e., six for P2 elements) and n_{broken} is the number of nodes that have broken, then the PC scheme operates only if $0 < n_{\text{broken}} < n_{\text{fault}}$. The PC scheme will basically find the tangentail tractions, $\vec{T}^n_{ik_T}$, in the unbroken nodes, given the boundary condition applied in the broken nodes for the same time step. Thus, the procedure will only influence the two interacting elements sharing the same breakable portion of the fault surface.

[37] Our PC scheme is simple and converges fast: when a fault node breaks in a given element, the modulus of its tangential traction is set to τ_c^n (condition (25)). Once this condition applies, the predicted tangential tractions $\vec{T}^n_{ik_T}$ in the unbroken nodes of the same element must be recomputed accordingly via (24). For this purpose, a new mass matrix, $\mathcal{K}^{\text{unbroken}}_{e_\Gamma}$, must be constructed considering only the unbroken fault nodes while for the broken nodes the tangential traction condition is set. If the magnitude of the new-predicted tractions overcomes the fault strength, then it is corrected by setting it to τ_c^n. This updating cycle continues iteratively through new predictions and corrections until no other node breaks inside the element after the last correction. The maximum number of possible iterations is given by the order of approximation, i.e., DOF, used in the fault elements, and will always be smaller than n_{fault} (i.e., five or less iterations for P2 elements). The PC procedure has to be performed locally in each piece of fault surface. It is an efficient iterative verification of boundary conditions and represents an additional reason to preserve low interpolation orders (i.e., P2 specifically) in the tetrahedra sharing a fault segment.

[38] Since the DG schemes do not enforce continuity of the fields between two adjacent tetrahedra, and the accuracy of our method depends on the special treatment of velocities over the fault, we must take care of the fault normal tractions in the same manner as for the tangential components. We now derive a formula to compute the normal traction, $\vec{T}^n_{ik_N}$, which ensures continuity of the fault normal velocity field. This model constrain is given by the jump condition (11).

[39] As done for the tangential slip rate (23), definition (7) may be written as

$$\vec{V}^{n+\frac{1}{2}}_{ik_N} := \vec{v}^{n+\frac{1}{2}}_{i_N} - \vec{v}^{n+\frac{1}{2}}_{k_N} = \vec{V}^{n-\frac{1}{2}}_{ik_N} + \vec{R}^n_{i_N} - \vec{R}^n_{k_N} + \Delta t S_{ik}\left(\frac{1}{\rho_i V_i} + \frac{1}{\rho_k V_k}\right) \cdot (\mathcal{I}_3 \otimes \mathcal{K}_{e_\Gamma})^{-1}(\mathcal{I}_3 \otimes \mathcal{F}_e)\mathcal{T}^n_{ik_N}.$$

Using condition (11) to force continuity of the normal velocity, we then define the fault normal traction

$$\vec{T}^n_{ik_N} = \left(\frac{\rho_i\rho_k V_i V_k}{\Delta t S_{ik}(\rho_i V_i + \rho_k V_k)}\right)(\mathcal{I}_3 \otimes \mathcal{F}_e)^{-1}(\mathcal{I}_3 \otimes \mathcal{K}_{e_\Gamma}) \cdot \left(-\vec{V}^{n-\frac{1}{2}}_{ik_N} - \vec{R}^n_{i_N} + \vec{R}^n_{k_N}\right), \quad (26)$$

from which the fault normal stress is given by

$$\sigma^n_N = \vec{T}^n_{ik_N} \cdot \vec{n}.$$

The frictional strength, τ_c^n, can now be computed on every fault node using (12) as a function of both σ^n_N and the friction coefficient, μ^n, which depends on the fault slip, U^n (8), through the slip weakening law (13).

[40] Definitions given for the normal (26) and tangential (24) traction components finally allow us to update the velocity field in every fault node via equation (20).

3.2.2. Fluxes Across the Fault for the Stress Scheme (17)

[41] For the stress scheme and within the *i*-tetrahedron, the flux across the fault, $\vec{g}_i^{n+\frac{1}{2}}$, is computed using only the velocity field in that tetrahedron, through the equation (20), so that the flux is given by

$$\vec{g}_i^{n+\frac{1}{2}} = \mathcal{P}^T_{ik}\vec{v}_i^{n+\frac{1}{2}}. \quad (27)$$

[42] The simplicity of this flux stems from the computation of a unique traction vector on the fault that guarantees either the continuity or discontinuity of the velocity field depending on whether the fault has broken or not. This fault-flux approximation is equivalent to the one proposed by *Benjemaa et al.* [2009] for P0 elements, where the flux estimation is based on an energy balance consideration across the fault, but the simpler form of definition (27) is due to the continuity of the fault normal velocity implicit in the computation of $\vec{T}^n_{ik_N}$ through (26).

4. Rupture Model Verification, Convergence and Efficiency

[43] Verification of dynamic rupture models is a particularly difficult task. Since no analytical solution exists for the spontaneous rupture problem (i.e., closed form equations for the resulting motions), the only possible way to be confident of a given approach is the comparison of results for a well-posed rupture problem between various numerical techniques based on different approximations. This kind of exercise has been systematically performed in recent years by an international group of modelers [*Harris et al.*, 2009]. In this section we present results for two benchmark tests proposed by this group, TPV3 and TPV10 (see: http://scecdata.usc.edu/cvws/index.html), and compare them with those obtained with finite difference, finite element, spectral element, discontinuous Galerkin and spectral boundary integral methods. Based on these comparisons, we assess the numerical convergence rate of our method, its efficiency and determine numerical criteria to guarantee its accuracy.

4.1. The Problem Version 3 (TPV3)

[44] Consider the spontaneous rupture of a vertical right-lateral strike-slip fault embedded in a homogeneous full-space with P- and S-waves speeds of 6000 m/s and 3434 km/s, respectively, and density of 2670 kg/m^3. The fault is rectangular and measures 30 km in length by 15 km in width (Figure 2). Rupture nucleation happens in a 3 km by 3 km square region, centered both along-strike and along-dip,

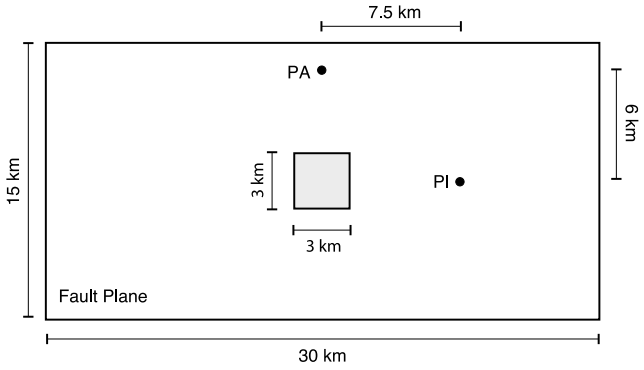

Figure 2. TPV3 rupture problem geometry. The gray square represents the nucleation patch, and the PA and PI dots represent the pure-antiplane and pure-inplane observational fault points, respectively.

because the initial shear stress there is higher than the fault strength. The friction law is linear slip-weakening with zero cohesion (Equations (12) and (13)), and both static and dynamic friction coefficients are constant over the fault. The initial fault normal traction is also constant, as are the static and dynamic fault strengths. Values for all source parameters, i.e., initial stress conditions and friction parameters, are shown in Table 1. Results for this problem are compared with those obtained by the DFM finite difference scheme [*Day et al.*, 2005], the ADER-DG discontinuous Galerkin scheme [*Pelties et al.*, 2012] and the spectral boundary integral equation method by *Geubelle and Rice* [1995] with the implementation of E.M. Dunham (MDSBI: Multidimensional Spectral Boundary Integral, version 3.9.10, 2008); all of them for an equivalent grid size of 50 m.

[45] All DGCrack solutions presented in this section were calculated for the same $100 \times 110 \times 95$ km^3 physical domain discretized with unstructured h-adaptive meshes such that the element characteristic lengths extends from 1 km in the CPML slab to the desired length over the fault plane (i.e., 1.0, 0.8, 0.5, 0.4, 0.3, 0.2 and 0.1 km).

[46] Our first comparison corresponds to the rupture times on the fault plane with the DFM method (Figure 3). We have used a characteristic elements size of 100 m over the fault (i.e., an effective grid size (internode distance) of about 50 m in our P2 elements approximation). The fit between both solutions is almost perfect. No significant difference may be seen in this comparison. Figure 4 compare DGCrack seismograms at fault points PI (pure in-plane deformation) and PA (pure anti-plane deformation) (see Figure 2) for the slip (4a), shear traction (4b) and slip rate (4c and 4d) fields with those obtained by the DFM, ADER-DG and MDSBI methods. Except for weak oscillations, the comparison is also excellent. Besides the stress build-ups, which are nicely resolved at both observational points before failure, let us notice how the friction law is well resolved as compared to the other solutions, with stress overshoots around 7 s and 8 s at PI, and 8.5 s and 10.5 s at PA. The associated slip reactivations are also well modeled and can be seen in the slip rate functions at both points. Stopping phases from the fault edges strongly determine the slip rate and are well resolved at 6.5 s and 7 s at PI, and at 4 s and 7.5 s at PA. A closer comparison of slip rates at both observational points (Figure 4d) suggests that the closest two solutions to each other correspond to ours and the one generated by the spectral boundary integral method (MDSBI). Despite weak oscillations present in the DFM, MDSBI and DGCrack waveforms, both amplitude and phase of the DGCrack and MDSBI solutions are remarkably similar.

[47] Since no analytic solution exists for this problem, quantitative comparisons between all the approximations may give insights about their correctness. Figure 5b presents a quantitative comparison of all numerical solutions based on cross-correlation, *cc*, measurements of the slip rate time series on both PI and PA observational points. Each colored square of the Cross-Correlation Matrix, *CCM*, corresponds to a *cc*-based metric between two solutions: for a given method, its metrics with respect to the other approaches are those corresponding to its associated raw and column of the matrix. Values in the upper triangular part of *CCM* are given by

$$CCM_{ij}^{\text{upper}} = \frac{cc_{ij} - cc_{\min}}{1 - cc_{\min}}, \tag{28}$$

where cc_{ij} is the maximum cross-correlation coefficient between the i and j solutions, and subscript min reads for the smallest coefficient of all possible combinations. Values in the lower triangular part of *CCM* are given by

$$CCM_{ij}^{\text{lower}} = \frac{dt_{ij} - dt_{\max}}{dt_{\max}}, \tag{29}$$

where dt_{ij} is the delay in seconds between the i and j solutions for the maximum correlation coefficient, and the max subscript means the maximum delay of all possible combinations. Both measures provide a quantitative mean to assess the similarity between solutions relative to the worst comparison found between all combinations. However, they do not provide absolute cross-correlation information except for the auto-correlations along the *CCM* diagonal. While the ADER-DG solution is the closest to both the DGCrack and MDSBI solutions in terms of correlation coefficients (see CCM^{upper} in Figure 5b), the smallest phase error is found between the DGCrack and MDSBI solutions (see CCM^{lower}). As may also be seen in Figure 4d, the solution with the lowest correlation metrics with respect to the other ones is that from DFM (i.e., first column and first row). By averaging both metrics per solutions couple, we may better assess which time series are the closest to each other. Figure 6 presents the results of this exercise, where the two discontinuous Galerkin solutions reveal to be the more similar, although very close to the one yielded by the Boundary Integral method. Measures provided by this method should be interpreted carefully since

Table 1. On-Fault Frictional and Stress Parameters for TPV3[a]

Fault Parameters	Nucleation	Outside Nucleation
Static friction coefficient, μ_s	0.677	0.677
Dynamic friction coefficient, μ_d	0.525	0.525
Slip weakening distance, δ_0 (m)	0.40	0.40
Initial shear stress, τ_0 (MPa)	81.6	70.0
Initial normal stress, σ_0 (MPa)	120.0	120.0

[a]The initial shear stress points to the along-strike direction. Medium properties outside the fault represent an infinite barrier.

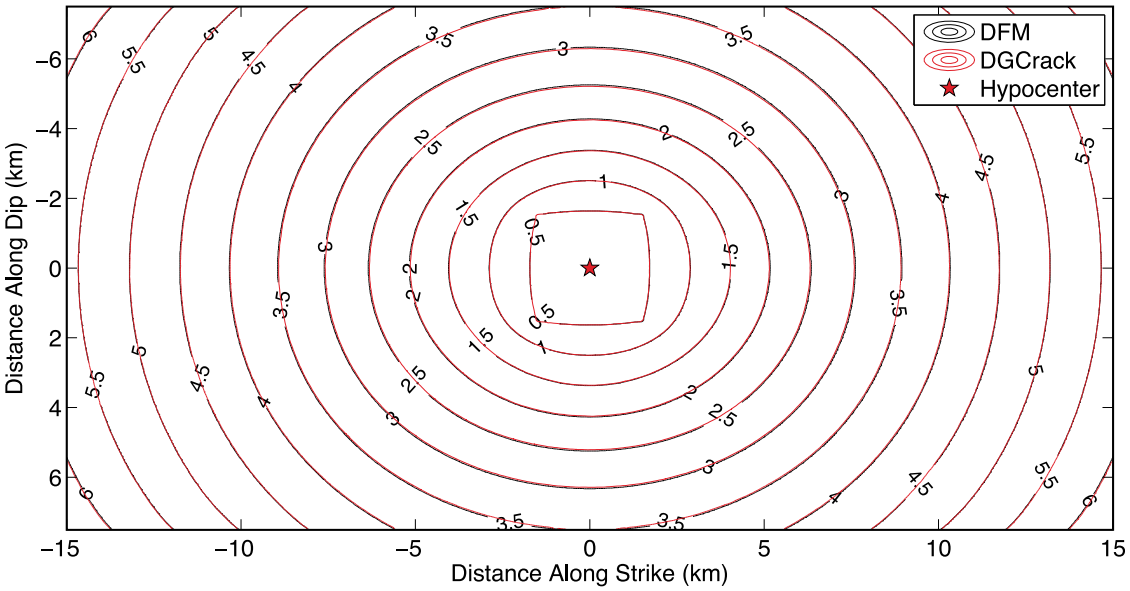

Figure 3. Comparison of rupture times for TPV3 yielded by the DGCrack and DFM [*Day et al.*, 2005] methods, both with an effective mesh increment of 50 m (i.e., 100 m fault elements for DGCrack).

they do not account for the computational cost required by each method to achieve its solution.

[48] One important issue in dynamic rupture modeling is the control of spurious oscillations produced by the advance of the crack tip throughout the discrete lattice. Using either artificial viscosity or intrinsic dissipation procedures in rupture models is a delicate matter because the associated damping does not distinguish between numerical and physical contributions. In other words, if badly handled, dissipation may absorb frequencies belonging to the physical-problem bandwidth affecting, for instance, peak slip rates and rupture speeds, as shown by *Knopoff and Ni* [2001]. This is probably why the ADER-DG scheme [*de la Puente et al.*, 2009], which uses intrinsically dissipative Godunov fluxes [*LeVeque*, 2002; *González-Casanova*, 2006], requires high interpolation orders to achieve good accuracy (e.g., compare O2 with O3 or higher order solutions in *Pelties et al.* [2012]). In the DGCrack scheme, in contrast, the centered flux scheme is conservative such that the energy is not intrinsically dissipated [*Hesthaven and Warburton*, 2008] but, because it is dispersive, contains spurious oscillations. However, since these oscillations remain reasonable small and we expect them to be even smaller for physically attenuating media or different friction laws (e.g., rate- and state-dependent), we have decided not to integrate an artificial viscosity.

[49] The upper horizontal axis in the Figures 5a and 5c represents the number of fault elements in the cohesive zone, N_c, associated to the characteristic element sizes shown in the lower horizontal axis. The cohesive zone is the fault area next to the crack tip where the shear stress drops from its static to its dynamic value. N_c is measured along the rupture-front propagation direction and its values correspond to the reference DFM solution for $h = 50$ m reported in *Day et al.* [2005].

[50] To assess the convergence rate of the DGCrack scheme and to determine a quantitative criterion that guaranties its accuracy, Figures 5a and 5c present two different error metrics, defined by *Day et al.* [2005] as the relative root mean square difference between a given solution and the reference one (i.e., the DFM solution for $h = 50$ m), as a function of the characteristic elements size on the fault. These metrics correspond to the rupture times over the fault and the peak slip rates at fault points PA and PI (Figure 2). Both figures reveal a power law convergence rate of the DGCrack method with regression exponents reported in Table 2 and compared to those for other methods. We also report in that table the exponent for the final slip on both observational points (not shown in the figure). It is important to notice that all DGCrack solutions presented in the manuscript correspond to unstructured meshes with refinements around the rupture surfaces. As mentioned by *de la Puente et al.* [2009], this is a critical issue since the accuracy of solutions significantly depends on the quality of the tetrahedral lattice built independently using standard tools (in this work we have used the Gmsh software developed by *Geuzaine and Remacle* [2009]), as can been seen in the error dispersion on both Figures 5a and 5c with respect to the regression lines.

[51] The accuracy of dynamic rupture models depends on the resolution of the cohesive zone, which may vary during rupture evolution. N_c is thus the numerical criterion that guaranties a given accuracy level. Figures 5a and 5c also reveal that one or more fault elements inside the cohesive zone (i.e., $N_c \geq 1$) is enough to achieve errors smaller than 1% and 10% for rupture times and peak slip rates, respectively. In the TPV3 test case, this condition implies fault element sizes smaller or equal to ~450 m.

[52] We finally address a fundamental question in computational sciences: the numerical efficiency. *Pelties et al.* [2012] have recently introduced a method to solve the dynamic rupture problem based on a discontinuous Galerkin scheme that incorporates a sophisticated strategy allowing arbitrarily high order approximations in space and time, i.e., the ADER-DG method. Since both the DGCrack and ADER-DG methods share many different capabilities linked

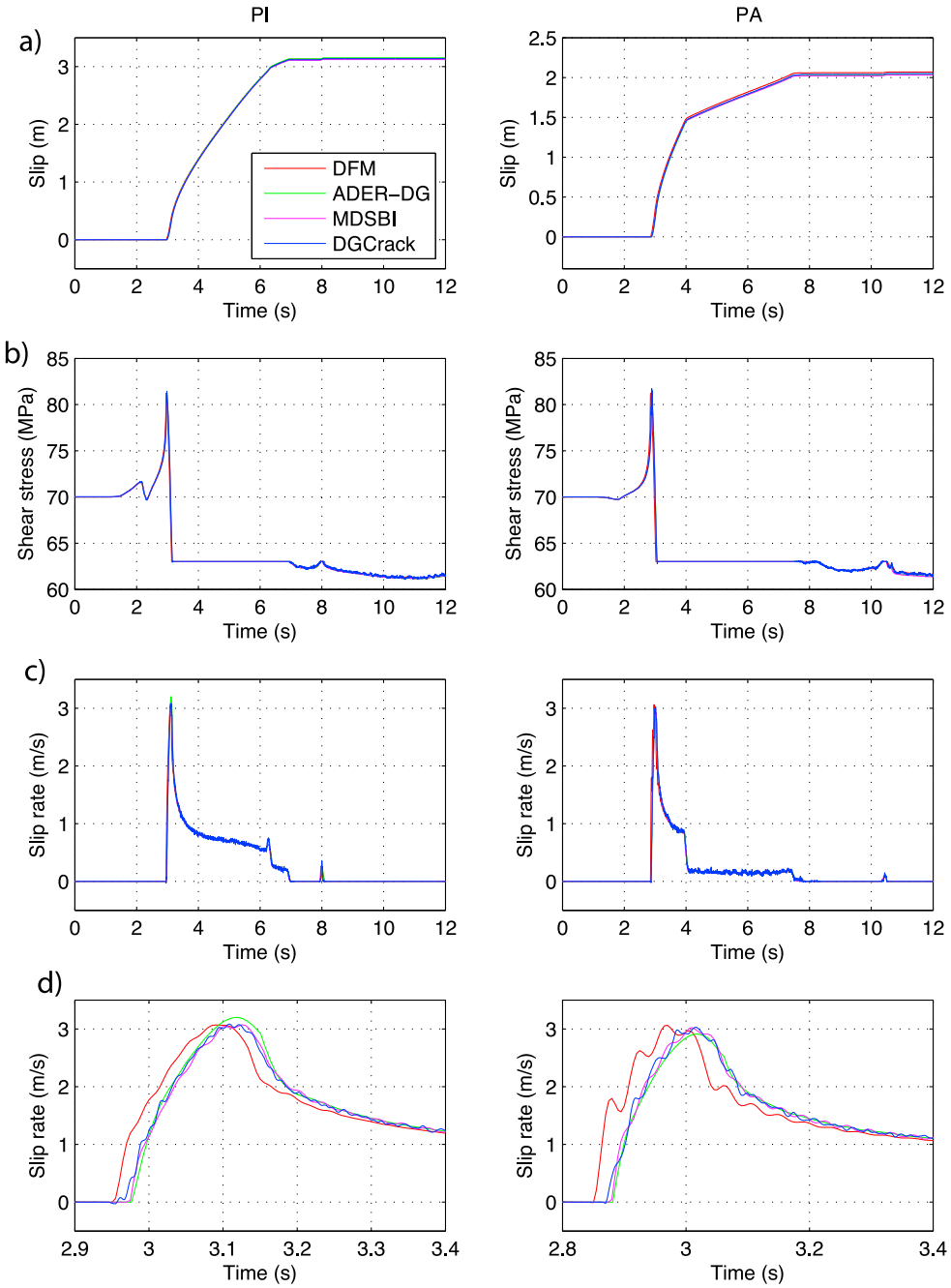

Figure 4. Comparison of on-fault time histories at PI (left column) and PA (right column) for (a) the slip, (b) the shear stress, and (c and d) the slip rate produced by four different numerical methods (inset legend: DFM, *Day et al.* [2005]; ADER-DG and MDSBI, *Pelties et al.* [2012]), all of them with an effective grid size of 50 m.

to the DG approximation, it is worth comparing their differences and to estimate the computational cost of each method to achieve the same accuracy level. Since the ADER-DG method is based on a modal approximation, the fluxes across the element faces are sensitive to all modes across the element. In a nodal approximation, however, like in the DGCrack method, they only depend on the nodes lying on the element face where the flux is computed. This difference translates into fewer computations in the nodal approximations [*Hesthaven and Warburton*, 2008]. Figure 5d presents a quantitative comparison of rupture times errors as a function of total computing times (i.e., the CPU time, which is given by the duration of each simulation multiplied by the number of cores) for both methods. The DGCrack simulations were run on a parallel computer with 172 cores (2.33 GHz quad-core Xeon processors) of the Department of Seismology at UNAM. Since the computational cost is not reduced by the ADER-DG method when using high

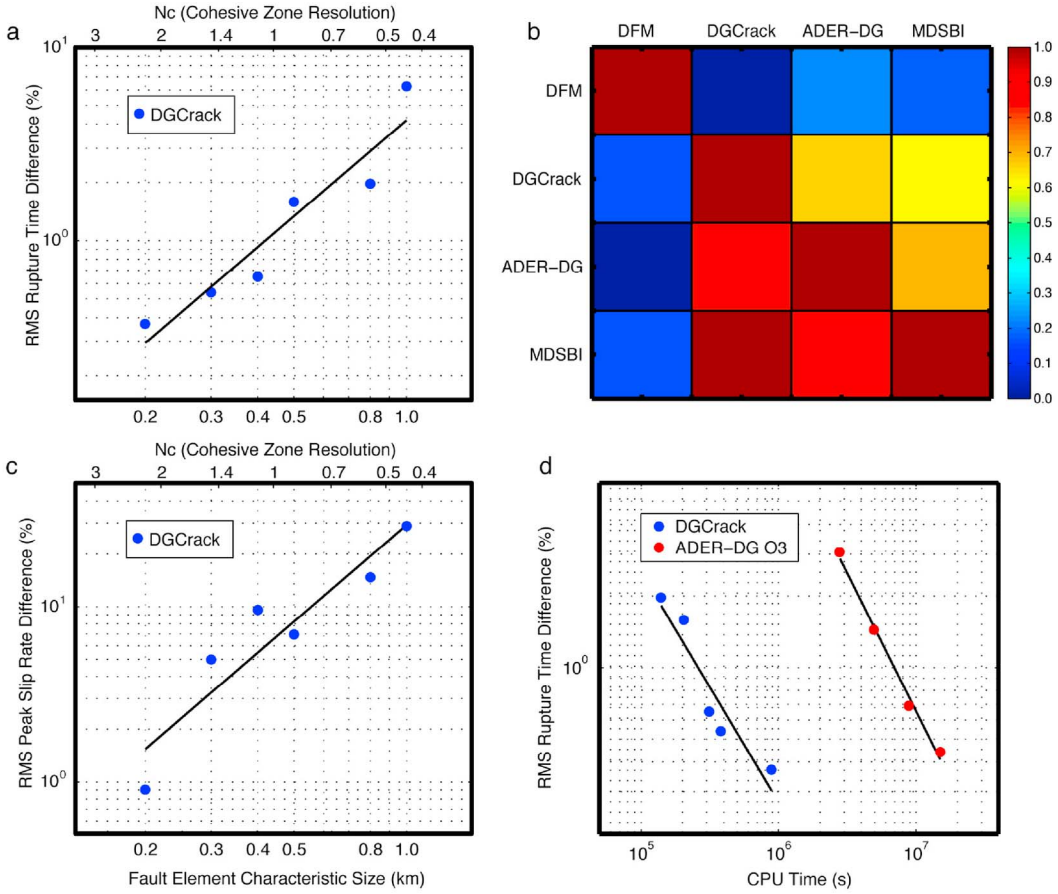

Figure 5. DGCrack convergence, accuracy and efficiency analysis based on TPV3 solutions. (a and c) Frames show regression lines with the power convergence rates for two error metrics with exponents reported on Table 2 for unstructured meshes, as a function of both the characteristic fault-element size (lower axis) and the cohesive zone resolution (upper axis). (b) Frame presents a cross-correlation based comparison between four different methods (see text). (d) Frame shows CPU total-time regressions yielded by the DGCrack and ADER-DG [*Pelties et al.*, 2012] methods for the same accuracy range. Since the DGCrack simulations were run in a faster computing platform, time differences should be divided by a factor of ∼3 to obtain actual values (see text).

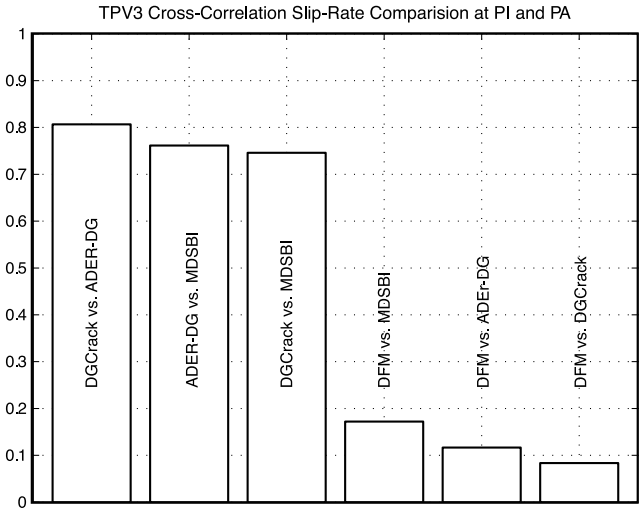

Figure 6. Averages of the cross-correlation measurements between pairs of solutions of Figure 5b yielded by four numerical methods.

approximation orders [*Pelties et al.*, 2012], values reported in Figure 5d correspond to the ADER-DG O3 solution. Both regression lines have about the same slope; so similar CPU time differences between the methods are expected for any grid size. If we take the same accuracy level used to establish the N_c condition in the last paragraph (i.e., 1% error for rupture times) then the CPU time of the ADER-DG O3

Table 2. TPV3 Convergence Rate Exponents for Different Methods and Error Metrics

Method	Rupture Times	Final Slip	Peak Slip Rate
DGCrack	1.65	1.52	1.83
ADER-DG 03[a]	2.84	0.99	0.80
DFM[b]	2.96	1.58	1.18
BI[b]	2.74	1.53	1.19
SGSN[c]	-	1.63	0.70

[a]*Pelties et al.* [2012].
[b]*Day et al.* [2005].
[c]*Dalguer and Day* [2007].

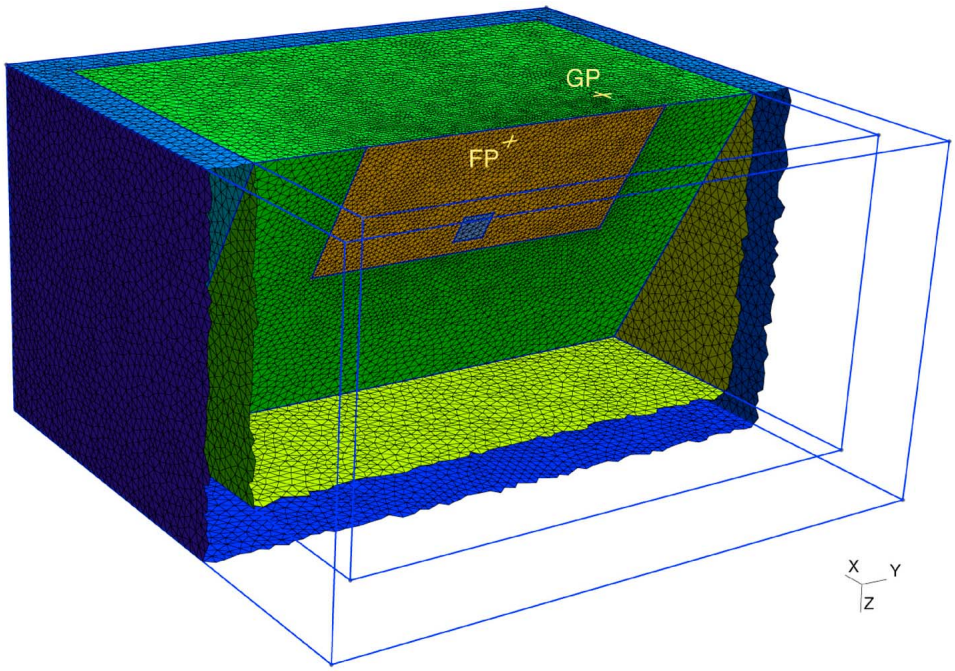

Figure 7. TPV10 60° dipping normal-fault (orange rectangle) problem geometry discretized with an unstructured mesh. The CPML slab is discretized by the blue tetrahedra while the physical domain by the green tetrahedra. The blue square represents the nucleation patch, and the yellow crosses represent the fault point (FP) and hanging wall free-surface ground point (GP) where solutions were obtained and compared (see Figure 9).

method is about 30 times larger than the one required by the DGCrack method in our computing platform. Since the simulation times reported by Pelties et al. were obtained using a 0.85 GHz BlueGene parallel computer, the actual CPU time difference would be reduced to a factor of ∼10 if both methods were run on the same platform, which still is a significant factor, especially if multiple large scale simulations are required. This comparison was made with the available data reported by *Pelties et al.* [2012], however it would be interesting to design a speed test of dynamic rupture simulations that could better reflect the CPU time required by both schemes. Besides, it is important to notice that ADER-DG shows smooth time series on the fault and accurate wave propagation away from it [*Dumbser and Käser*, 2006]. Theses characteristics are not quantified here and may be essential for long-range wave propagation problems.

4.2. The Problem Version 10 (TPV10)

[53] Our last verification test consists of a 60° dipping normal fault reaching the free surface of a homogeneous half-space (Figure 7) with P- and S-waves speeds of 5716 m/s and 3300 km/s, respectively, and density of 2700 kg/m^3. The fault has the same dimensions as in TPV3 (i.e., 30 km, 15 km wide) but the center of its 3 × 3 km^3 nucleation patch is located deeper, at 12 km along dip. Frictional and initial stress conditions on the fault plane are reported in Table 3, where the cohesion term of equation (12) is not zero, and both pre-stress conditions are dependent on the along-dip distance, h_d. The unstructured h-adaptive tetrahedral mesh used to obtain the DGCrack solution in shown in Figure 7, which has a characteristic element size of 100 m over the fault plane.

[54] This test case has interesting features that are essential to verify a dynamic rupture model for non-planar faults. Since we deal with a dipping normal fault reaching the Earth's surface, reflected waves are bounced back to the source, inducing transient variations of the fault traction vector that significantly affect rupture propagation via the Coulomb failure criterion (12) [*Nielsen*, 1998; *Oglesby et al.*, 1998]. Figure 8 presents a comparison of rupture times over the fault obtained with three different methods [*Harris et al.*, 2009]: a finite element (FaulMod; *Barall* [2009]), a spectral element (SPECFEM3D [*Kaneko et al.*, 2008]) and the DGCrack methods. The three solutions were computed with a fault elements size of 100 m. Despite the complexity of the rupture

Table 3. On-fault frictional and stress parameters for TPV10[a]

Fault Parameters	Nucleation	Outside Nucleation
Cohesion, C (MPa)	0.20	0.20
Static friction coefficient, μ_s	0.760	0.760
Dynamic friction coefficient, μ_d	0.448	0.448
Slip weakening distance, δ_0 (m)	0.50	0.50
Initial normal stress, σ_0 (MPa)	$0.007378h_d$	$0.007378h_d$
Initial shear stress, τ_0 (MPa)	$C + \sigma_0(0.0057 + \mu_s)$	$0.55\sigma_0$

[a]The initial shear stress points to the along-dip direction. h_d is the along-dip distance measured in meters from the free surface. Medium properties outside the fault represent an infinite barrier.

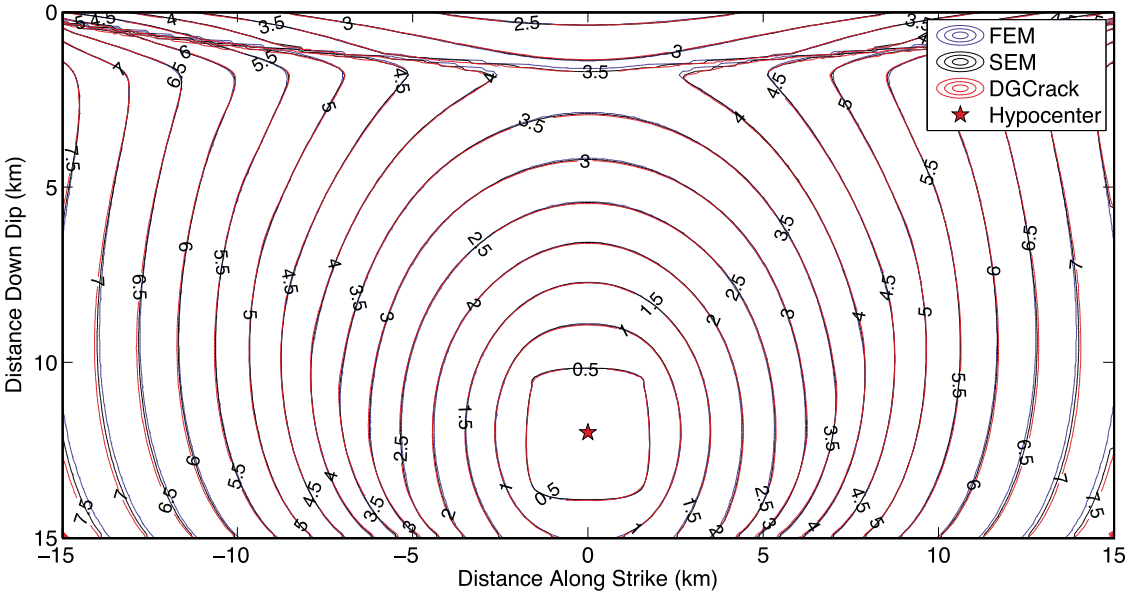

Figure 8. Comparison of rupture times for TPV10 yielded by the DGCrack, FEM [*Barall*, 2009] and SEM [*Kaneko et al.*, 2008] methods, all of them obtained with an effective mesh increment over the fault of 100 m.

model, the match between all solutions is remarkably good. Dynamic effects on rupture propagation due to the presence of the free surface are clearly seen in the upper most 2 km, where a secondary rupture front propagating down-dip is initiated about 2.5 s after nucleation.

[55] Figure 9 shows on- and off-fault waveforms computed by the same three methods with (lower traces) and without (upper traces) low-pass filtering at 3 Hz. From top to bottom, the left column presents the time evolution of the slip rate, shear stress and normal stress at fault point FP (Figure 7), which is aligned along strike with the center of the nucleation patch and located 1.5 km from the free surface along dip. On-fault solutions reveal that the best fits along the entire waveforms correspond to the DGCrack and SEM signals during the first 10 s, and to the DGCrack and FEM signals during the remaining 5 s. This suggests that, despite the spurious oscillations present in the latter part of the DGCrack waveforms, this method provides the most robust solution for this problem compared to the SEM and FEM methods. The right column of Figure 9 shows, from top to bottom, the two horizontal components (i.e., fault parallel, FP, and fault normal, FN, components) of the ground velocity and vertical displacements at the ground point GP (Figure 7), which is located 3 km in the along strike direction from the fault extremity and 3 km away from the fault trace on the hanging wall. In the ground motion synthetics the situation is slightly different. The closest two solutions along the entire records are those produced by the DGCrack and FEM methods (see filtered velocities and displacements up to 10 s). Although both the DGCrack and SEM solutions present spurious oscillations, the 3 Hz low pass filter did not eliminate longer-period oscillations in the DGCrack seismograms, particularly present after 10 s. Since similar noise is found in the on-fault seismograms, this inaccuracy is probably due either to long-range numerical dispersion associated with the centered fluxes across the fault or wave reflections associated with the mesh coarsening around the fault surface.

5. Rupture Along the 1992 Landers-Earthquake Fault System

[56] The 28 June 1992 Landers earthquake (Mw 7.3) in southern California produced one of the most valuable data sets ever recorded. The amount and diversity of geophysical observations allowed constraining the earthquake rupture history, revealing a large complexity of the slip pattern in a wide frequency range (<0.5 Hz) [e.g., *Campillo and Archuleta*, 1993; *Wald and Heaton*, 1994; *Olsen et al.*, 1997; *Hernández et al.*, 1999]. The large rupture size (80 km long, 16 km wide), the long rupture duration (>20 s) and the intricate fault-system geometry bring an exceptional opportunity to test our discontinuous Galerkin source model. However, to fully understand the detailed rupture process of the Landers earthquake deserves an extensive analysis that goes beyond the purpose of this work. For this reason we shall mainly use this study case for illustrating the capabilities of the DGCrack approach in realistic conditions, and to elucidate some essential aspects of such an event related to the initial stress conditions along the fault.

[57] The Landers earthquake broke four main right-lateral faults, namely the Johnson Valley, Homestead Valley and Emerson and Camp Rock faults, which are connected through jogs and step-overs (Figure 12b) forming a complex nonplanar fault system (Figure 10 and red segment in Figure 12b). The detailed fault geometry was taken from the Community Fault Model for Southern California [*Plesch et al.*, 2007], which essentially consists of several strike-slip vertical segments, as shown in Figure 12b with grey dots. To discretize the model we considered a 1D layered medium [*Wald and Heaton*, 1994] (see L1, L2 and L3 layer boundaries on Figure 10) and took advantage of the hp-adaptivity.

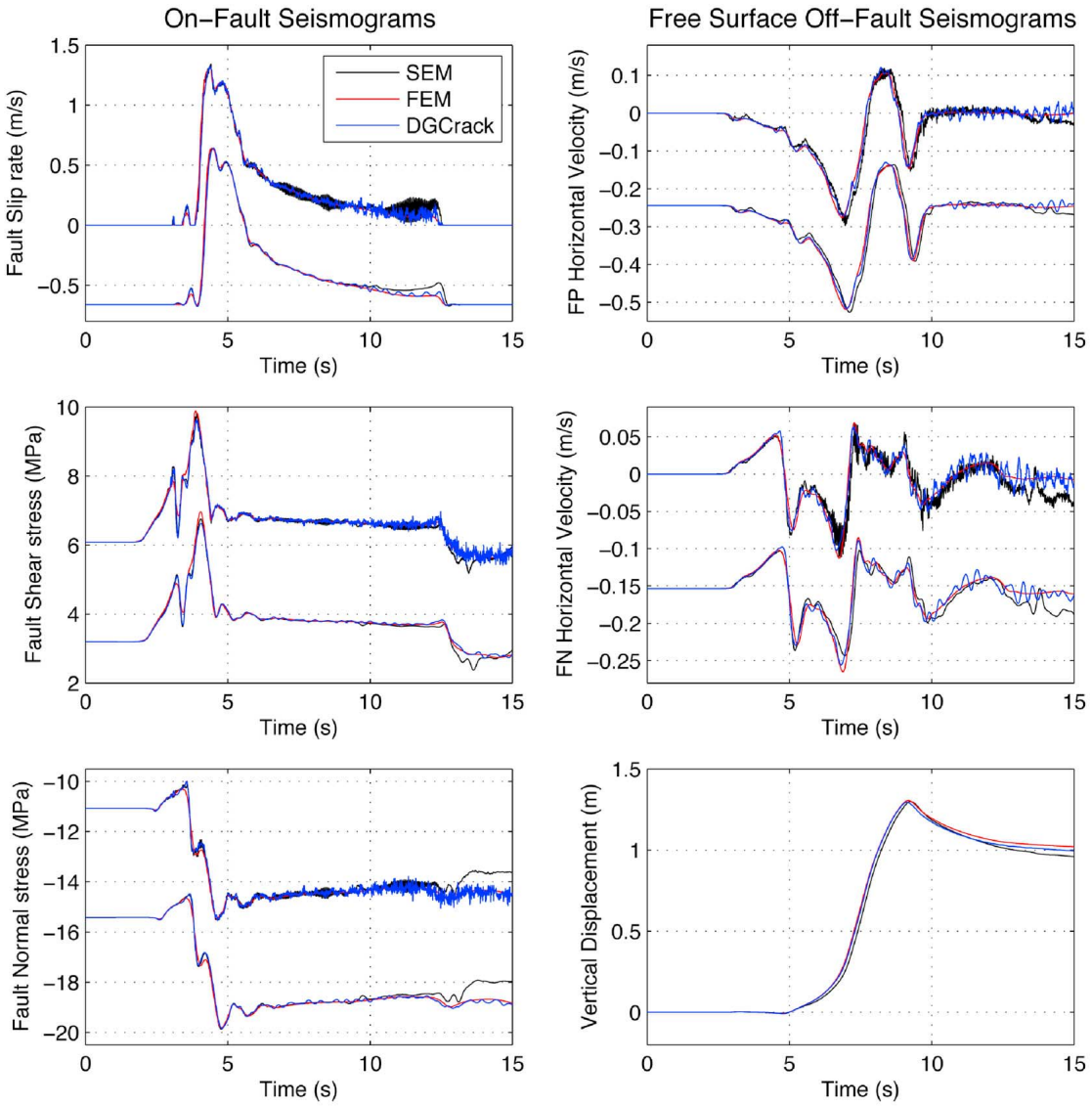

Figure 9. TPV10 (left) on-fault at FP and (right) off-fault at GP (see Figure 7) waveforms comparison for three methods (inset) with (lower traces) and without (upper traces) 3 Hz low-pass filtering.

This means that we refined the mesh around the rupture surface and simultaneously adapted the bulk elements sizes to resolve 0.5 Hz waves according to each layer properties, so that the wave-propagation accuracy criterion determined by *Etienne et al.* [2010] is largely satisfied (i.e., five elements per minimum wavelength). The gradual mesh coarsening from 300 m over the fault to 1100 m throughout the CPML region produced a discrete lattice with 4.48 millions tetrahedra, from which 48.6% are P1 elements and belong to the CPML slab (Figure 10), and the rest (51.4%) are P2 elements and discretize the physical domain. Dimensions of the computational volume are $67.0 \times 101.6 \times 29.0$ km^3 in the x, y and z directions, respectively, such that to complete a 20 s simulation, the DGCrack model spent a total CPU time of 1.73×10^6 s, which correspond to 9.6 hours in 50 cores of our Pohualli parallel platform.

[58] The initial stress conditions in the fault (i.e., pre-stress conditions) correspond to the initial shear tractions, τ_0, determined by *Peyrat et al.* [2001] on a planar fault (Figure 12a), which represent an improved version of those used by *Olsen et al.* [1997]. To estimate these initial conditions, they computed the static stress change in a planar fault associated with the total slip found by *Wald and Heaton* [1994] (Figure 12d), reversed its sign and added a homogeneous tectonic field of 5 MPa. *Peyrat et al.* [2001] also considered a constant static fault strength $\tau_s = \sigma_0 \cdot \mu_s = 12.5$ MPa, $\mu_d = 0.0$, and an upper bound for τ_0 equal to $0.95 \cdot \tau_s$ everywhere on the fault. We proceed in the same way except in the uppermost 2.5 km, where we obtained unreasonable large slips in our first simulations. For producing reasonable simulation results, we thus lowered the upper bound of τ_0 to $0.9 \cdot \tau_s$ over the whole fault and multiplied τ_0 by a linear taper going from 1 at 2.5 km depth to 0 at the free surface. Instead of searching suitable friction coefficients to explain the observed ground motions as done in previous studies [*Aochi and Fukuyama*, 2002; *Aochi et al.*, 2003] we simply set them homogeneous over the fault such that both the strength excess and the dynamic stress drop exactly match those considered by

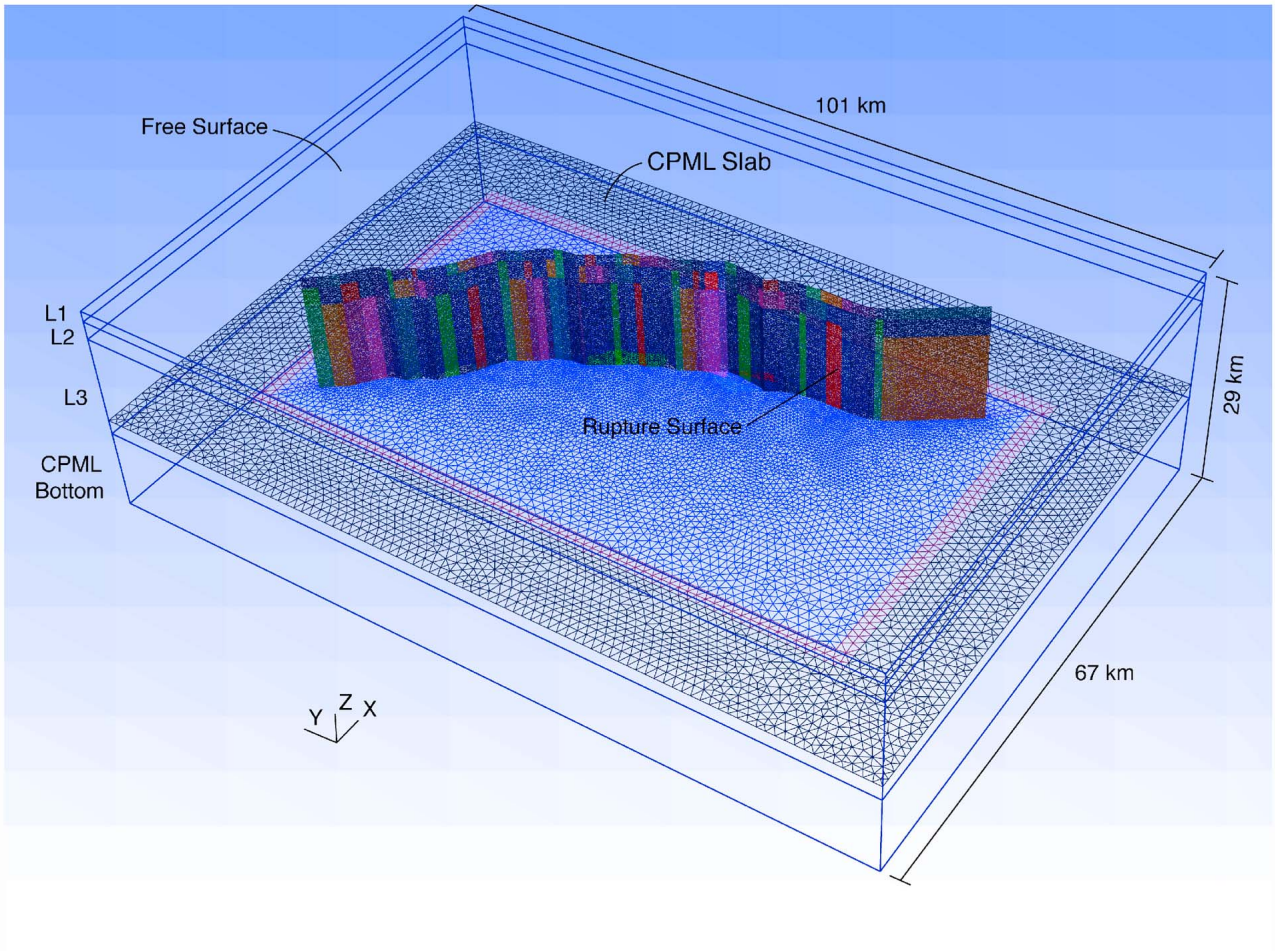

Figure 10. The 1992 Landers earthquake fault-system geometry embedded in a 1D layered medium (L1, L2 and L3) and discretized with an hp-adaptive tetrahedral mesh (see text).

Peyrat et al. [2001], except in the shallow part where the taper was applied and within those small regions where the initial shear stress was upper bounded to $0.9 \cdot \tau_s$. As expected when including the real fault geometry, to allow spontaneous rupture propagation through the stepovers and fault kinks we had to reduce fracture energy by a factor of two as compared with *Peyrat et al.* [2001] model by setting δ_0, the stress breakdown slip (i.e., the slip-weakening distance (13)), equal to 40 cm instead of 80 cm. Rupture was nucleated in a 7 km deep circular patch with 1 km of radius [*Olsen et al.*, 1997] located 67 km from the northern fault edge in the along-strike direction [*Wald and Heaton*, 1994] (Figure 12a). To initiate a sustained rupture, we raised the initial shear stress 5% above the fault strength in that patch. As a result, an initial stress-drop kick of about 0.6 MPa initiated the earthquake.

[59] Figure 11 shows a series of snapshots of the slip rate (left column) and shear stress (right column) on the fault during rupture propagation. Interesting rupture patterns appeared in the rupture process, as reflected waves in the layers interfaces (2.9 s snapshot), rupture front jumps (5.1 s snapshot) and bifurcations (7.9 s snapshot), and supershear fault segments (11.3 s snapshot), among others.

[60] Previous models of the Landers earthquake have shown that considering both the fault system geometry and the heterogeneities of the surrounding medium is critical to explain different geophysical observations [e.g., *Fialko*, 2004; *Cianetti et al.*, 2005; *Cruz-Atienza*, 2006]. Our results (Figures 11 and 12) lead to the same conclusion. If the fault geometry did not play a major role during the earthquake, both the initial stress conditions and frictional parameters adopted by *Peyrat et al.* [2001], which were determined assuming a planar rupture surface [*Olsen et al.*, 1997], would have been valid over the real fault-system geometry. Instead, the fault geometrical barriers (i.e., kinks) strongly affect the energy budget, making the spontaneous rupture propagation more difficult. The effect of fault geometry into that budget is clear in our results, since we had to reduce the planar-fault fracture energy by a factor of two to allow rupture propagation along the entire fault system. It can be said that half of the amount of energy that *Peyrat et al.* [2001] found to be dissipated through cohesive forces (i.e., frictional work) with constant normal tractions seems to be related with other physical mechanisms promoting energy leakage possibly related to the fault geometry, such as off-fault anelastic processes [*Duan and Day*, 2008] or high frequency radiation associated with changes of rupture speed and direction in the vicinity of the fault kinks [*Adda-Bedia and Madariaga*, 2008].

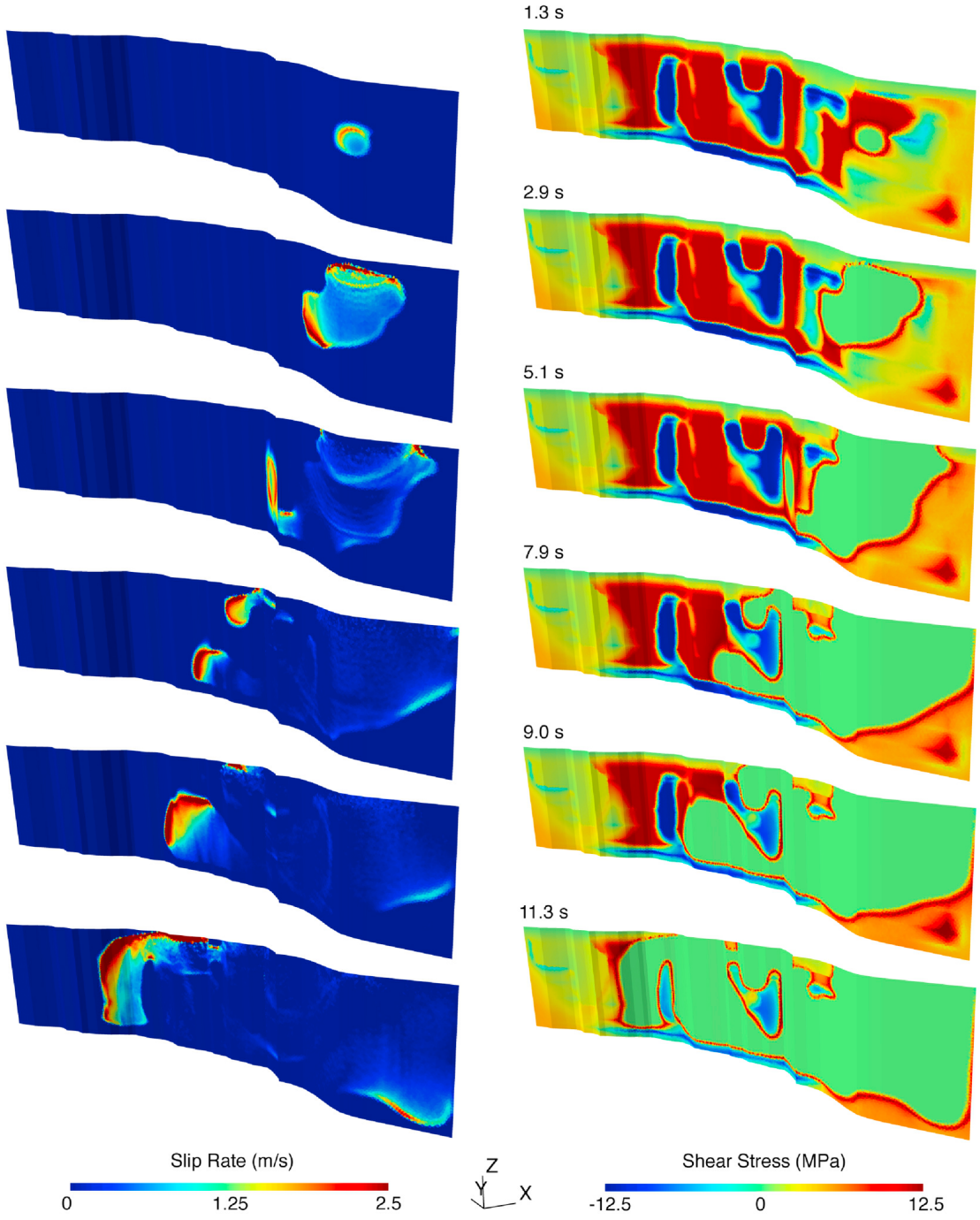

Figure 11. Landers earthquake dynamic rupture simulation results. (left) Slip rate and (right) shear stress snapshots over the non-planar fault system (Figure 10) for different times of the rupture process.

[61] Figure 12 finally shows a comparison between the final slip determined by *Wald and Heaton* [1994] over a three planar fault segments projected into a single plane (Figure 12d) and the one yielded by our simulation deployed over a plane (Figure 12c). There is clearly an underestimation of the seismic moment in our model, which is based on the static stress change produced by the final slip of *Wald and Heaton* [1994] in a planar fault [*Olsen et al.*, 1997]. Notice that both fault segments where the final slip is dramatically underestimated are either confined between (i.e., Kickapoo stepover) or overlapping (i.e., stepover joining the Homestead Valley and Emerson faults) fault kinks. Since the final slip we obtained is so different to the one found by *Wald and Heaton* [1994] that explains a large set of observed data (e.g., regional seismograms and GPS records), we do not expect our earthquake model to be realistic (i.e., to fit the ground surface observations). This finally leads us to conclude that a realistic dynamic source model of

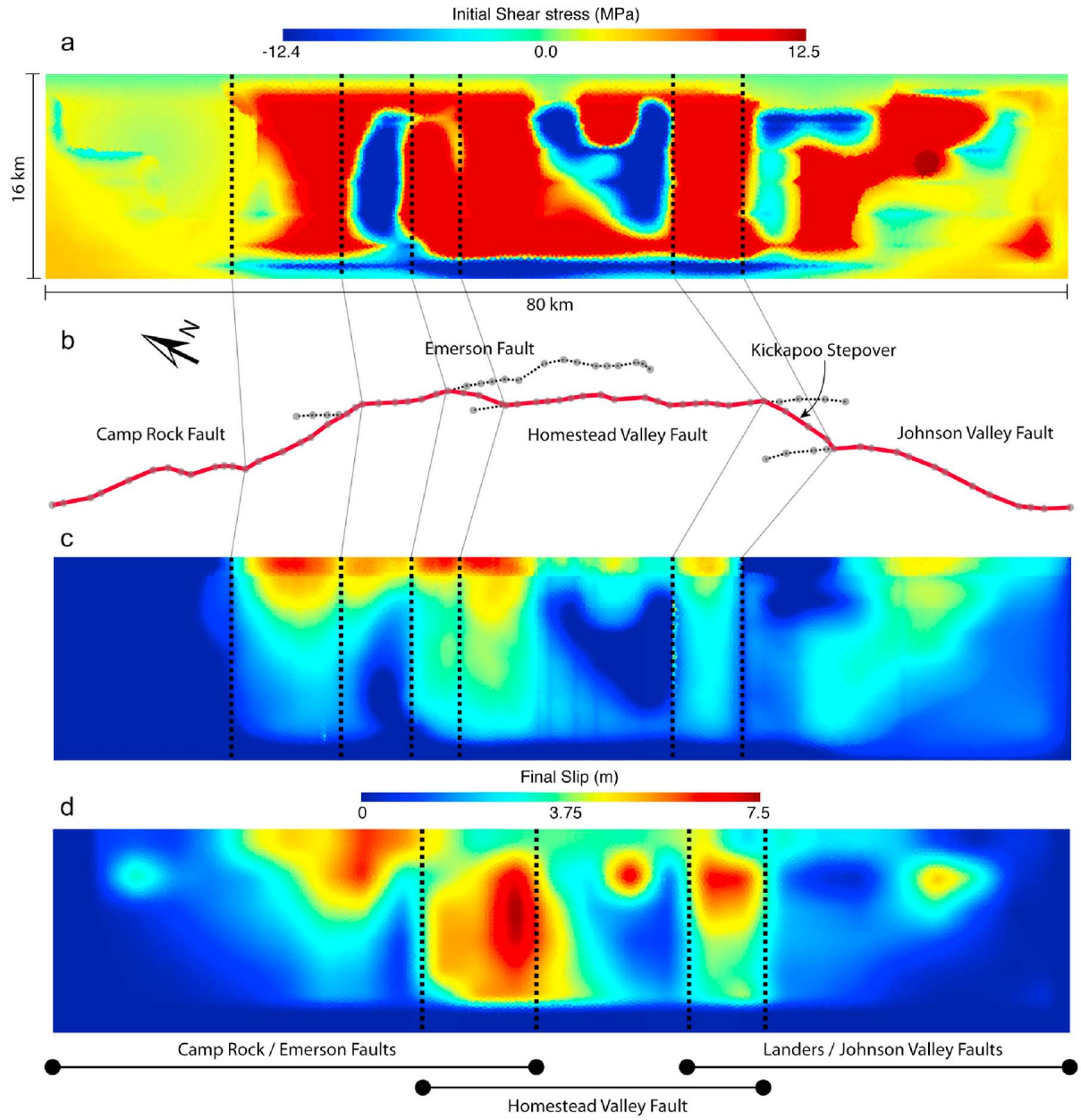

Figure 12. Landers earthquake fault parameters displayed in a single plane with major geometrical barriers (i.e., kinks) indicated with black dotted lines. (a) Initial shear stress used in this study; (b) discretization (grey dots) of the Landers earthquake fault system taken from the Community Fault Model for Southern California [*Plesch et al.*, 2007]. The red line indicates the fault geometry used in this study (Figure 10); (c) final slip produced by the DGCrack dynamic rupture simulation; and (d) final slip and fault discretization for the 1992 Landers earthquake found by *Wald and Heaton* [1994].

the Landers earthquake may only be constructed by considering its real and intricate fault geometry when determining the initial fault-traction conditions.

6. Conclusions

[62] In this work we have introduced a novel discontinuous Galerkin method, the DGCrack, to simulate the dynamic rupture propagation of earthquakes in 3D along faults with intricate geometries (i.e., non-planar). The method is hp-adaptive, which means that the elements of the unstructured tetrahedral mesh discretizing the simulation domain may adapt both their sizes (h-adaptivity) and approximation orders (p-adaptivity) depending on the problem geometry and the medium properties (i.e., P0, P1 or P2 elements in the wave propagation domain, and P2 elements over the fault). To guarantee a fast convergence rate, our scheme imposes the dynamic-rupture boundary conditions through *ad hoc* fluxes across the fault that verify both the jump conditions introduced by *Day et al.* [2005] and an additional condition

forcing the continuity of the fault-normal velocity field. The jump conditions imply the continuity of the tangential fault velocities on the fault nodes where rupture did not happen, and the collinearity of both the fault shear traction and the slip rate in those nodes where rupture has occurred. On the other hand, the additional condition guarantees the numerical stability and accuracy of the fault normal tractions required in the Coulomb slip-dependent friction law. For modeling rupture propagation throughout the interior of each fault element, we have introduced an efficient predictor-corrector scheme on these elements that accurately estimates the shear tractions at every fault node for every time step.

[63] A convergence analysis based on the SCEC-USGS TPV3 spontaneous-rupture benchmark has revealed power law convergence rates of the DGCrack method for three different fault-observable RMS error metrics [*Day et al.*, 2005], with exponents equal to 1.65 for rupture times, 1.52 for final slip and 1.83 for peak slip rates. These estimates are similar to those reported for well-established finite difference (DFM and SGSN), discontinuous Galerkin (ADER-DG) and boundary integral (BI) methods. We have obtained excellent results (i.e., rupture times and peak slip rate RMS errors smaller than 1% and 10%, respectively) provided that the cohesive zone is resolved by one or more fault elements (i.e., $N_c \geq 1$). For the TPV3 test case, this condition translates into fault element smaller or equal than $\sim$450 m. Since both the DGCrack and ADER-DG methods share many different capabilities linked to the DG approximation, we have assessed the difference in computational cost to achieve the same accuracy level for rupture times. We find that DGCrack is about 10 times faster than ADER-DG irrespectively of the mesh size if they were run in the same computing platform.

[64] Since no analytical solution exists for the spontaneous rupture problem, quantitative comparisons between different approximated solutions may give insights about the correctness of the numerical approaches to solve a given problem. We have thus introduced a simple way to assess the similarity among solutions for TPV3 generated by four different methods, based on the phase and cross-correlation coefficients of slip rate time series. Results of this exercise show that the DGCrack and ADER-DG discontinuous Galerkin solutions are the most similar, although very close to the one computed by the spectral boundary integral method (i.e., the MDSBI approach). As suggested by J. P. Ampuero (personal communication, 2012), this procedure may be systematically used to quantitatively compare approaches for different rupture problems like those undertaken by the international group of modelers promoted by SCEC-USGS (see http://scecdata.usc.edu/cvws/) [*Harris et al.*, 2009].

[65] To complete the verification of the DGCrack method, we have also solved TPV10 [*Harris et al.*, 2009], which consists of a 60° dipping normal fault reaching the free surface. This test case has interesting features that are essential to verify a dynamic rupture model for non-planar faults, because reflected waves in the Earth's surface are bounced back to the source inducing transient variations of the fault traction vector that significantly affect rupture propagation via the Coulomb failure criterion. Comparison of rupture times and both on-fault and ground-motion seismograms with those calculated by the SEM [*Kaneko et al.*, 2008] and FEM [*Barall*, 2009] approaches reveal a very good overall agreement among all solutions (especially between the DGCrack and FEM solutions), including the strong dynamic perturbations on the fault normal tractions close to the free surface. Numerical oscillations in the DGCrack solution are mainly present after 10 s of the earthquake nucleation, which is probably due either to long-range numerical dispersion associated with the centered fluxes across the fault or reflections associated with the unstructured mesh coarsening around the fault. However, since these oscillations remain reasonable small and we expect them to be even smaller for physically attenuating media [*Tago et al.*, 2010] or different friction laws (e.g., rate- and state-dependent), we have decided not to integrate an artificial viscosity into the scheme.

[66] We finally applied the DGCrack method to study some aspects of the 1992 Landers earthquake considering a realistic fault-system geometry. Our simulation deploy a 1D layered medium and took advantage of the hp-adaptivity by refining the unstructured mesh around the rupture surface and simultaneously adapting the elements sizes to resolve 0.5 Hz waves everywhere in the simulation domain. 48.6% of the 4.48 millions tetrahedra in the mesh are P1 elements and belong to the CPML slab, while the rest (51.4%) are P2 elements and discretize the entire physical domain. Our source model is based on a slightly modified version of the heterogeneous initial shear stress determined by *Peyrat et al.* [2001] on a planar fault from the final slip found by *Wald and Heaton* [1994]. Since both we had to reduce fracture energy by a factor of two with respect to the earthquake model proposed by *Peyrat et al.* [2001] to allow rupture propagation along the entire non-planar fault system, and obtained a significant seismic moment underestimation, we conclude that generating realistic pre-stress conditions for the Landers earthquake from its final slip distribution requires considering the fault-system geometry.

[67] Recent large subduction earthquakes have raised fundamental questions concerning the stability and segmentation of the subduction zones. To study this seismogenic regions accounting for more realistic physical behaviors, introducing into DGCrack both flexible friction laws (e.g., rate- and state-dependent) and the presence of fluids in the fault zone (i.e., thermal pressurization) would be essential in the near future.

Appendix A: DG-FEM Method for Wave Propagation

[68] To solve the hyperbolic system (1), which models the wave propagation in an elastic medium, we follow the DG-FEM method proposed by *Etienne et al.* [2010]. The method requires a discretization of the entire domain into sub-domains called elements. The DG-FEM is a mixture of two well-known methods: the Finite Element method (FEM), because it uses a space of basis functions and a space of test functions in each element [*Zienkiewicz et al.*, 2005], and the Finite Volume method (FVM), since the elements are decoupled from each other but integrated through the evaluation of fluxes across the elements faces [*LeVeque*, 2002]. The result of this combination is a method that ensures the geometric flexibility that supports local resolution adaptivity and that can deal with wave-dominated problems. However, the cost of having decoupled elements is

an increment of the total amount of degrees of freedom (DOF).

[69] For the space approximation we adopted the nodal form of the DG-FEM formulation, i.e., the solution in each element has a spatial support (nodes) that depends on the amount of degrees of freedom chosen for the discretization [*Hesthaven and Warburton*, 2008]. To approximate the stress and velocity vectors in the *i*-element we write

$$\begin{aligned}\hat{\vec{v}}_i(\vec{x},t) &= \sum_{j=1}^{d_i} \vec{v}_{i_j}(\vec{x}_j,t)\varphi_{i_j}(\vec{x}) \\ \hat{\vec{\sigma}}_i(\vec{x},t) &= \sum_{j=1}^{d_i} \vec{\sigma}_{i_j}(\vec{x}_j,t)\varphi_{i_j}(\vec{x}),\end{aligned} \tag{A1}$$

where $\vec{x} \in D_i$, t is the time and d_i is the number of nodes or DOF associated with the interpolation Lagrangian polynomial basis function φ_{i_j} relative to the j-node located at $\vec{x}_j$. This representation differs from the modal form in that the DOF, $\vec{v}_{i_j}$ and $\vec{\sigma}_{i_j}$, are space dependent.

[70] For the DG-FEM formulation we require a weak formulation of (1). The weak form makes the residual to be orthogonal to a space of test functions. The case when that space is the same as the space of interpolation functions is called Galerkin. To do so, we multiply (1) by a test function φ_{i_r} and integrate the system over the volume of the *i*-element

$$\begin{aligned}\int_{V_i} \varphi_{i_r}\rho\partial_t\vec{v}dV &= \int_{V_i} \varphi_{i_r} \sum_{\theta\in\{x,y,z\}} \partial_\theta(\mathcal{M}_\theta\vec{\sigma})dV \\ \int_{V_i} \varphi_{i_r}\Lambda\partial_t\vec{\sigma}dV &= \int_{V_i} \varphi_{i_r} \sum_{\theta\in\{x,y,z\}} \partial_\theta(\mathcal{N}_\theta\vec{v})dV \quad \forall r \in [1,d_i],\end{aligned} \tag{A2}$$

where V_i is the volume of the *i*-element.

[71] Integration by parts of the right side of (A2) leads to

$$\begin{aligned}\int_{V_i} \varphi_{i_r}\rho\partial_t\vec{v}dV &= -\int_{V_i} \sum_{\theta\in\{x,y,z\}} \partial_\theta\varphi_{i_r}(\mathcal{M}_\theta\vec{\sigma})dV \\ &\quad + \int_{S_i} \varphi_{i_r}\left(\sum_{\theta\in\{x,y,z\}} \mathcal{M}_\theta n_\theta\right)\vec{\sigma}dS \\ \int_{V_i} \varphi_{i_r}\Lambda\partial_t\vec{\sigma}dV &= -\int_{V_i} \sum_{\theta\in\{x,y,z\}} \partial\theta\varphi_{i_r}(\mathcal{N}_\theta\vec{v})dV \\ &\quad + \int_{S_i} \varphi_{i_r}\left(\sum_{\theta\in\{x,y,z\}} \mathcal{N}_\theta n_\theta\right)\vec{v}dS,\end{aligned} \tag{A3}$$

where S_i is the surface of the *i*-element and $\vec{n}$ is the outward pointing unit normal vector with respect to S_i.

[72] The second terms of the right-hand side of (A3) correspond to the fluxes of the stress and velocity wavefields across S_i. In the classical FEM, the fluxes are canceled between adjacent elements because the surface nodes are unique, i.e., the method enforces continuity of the wavefields. In contrast, since each element has its own nodes in the DG-FEM, the elements are coupled through the fluxes, similar to the FVM. To evaluate the fluxes, we chose the centered flux scheme for its computational efficiency and its non-dissipative property [*Remaki*, 2000; *Benjemaa et al.*, 2009; *Delcourte et al.*, 2009].

[73] Using the approximation (A1) and assuming constant physical properties per element, the weak formulation (A3) can be approximated as

$$\begin{aligned}\rho_i\int_{V_i} \varphi_{i_r}\partial_t\hat{\vec{v}}_i dV &= -\int_{V_i} \sum_{\theta\in\{x,y,z\}} \partial_\theta\varphi_{i_r}\left(\mathcal{M}_\theta\hat{\vec{\sigma}}_i\right)dV \\ &\quad + \frac{1}{2}\sum_{k\in N_i}\int_{S_{ik}} \varphi_{i_r}\mathcal{P}_{ik}\left(\hat{\vec{\sigma}}_i + \hat{\vec{\sigma}}_k\right)dS \\ \Lambda_i\int_{V_i} \varphi_{i_r}\partial_t\hat{\vec{\sigma}}_i dV &= -\int_{V_i} \sum_{\theta\in\{x,y,z\}} \partial_\theta\varphi_{i_r}\left(\mathcal{N}_\theta\hat{\vec{v}}_i\right)dV \\ &\quad + \frac{1}{2}\sum_{k\in N_i}\int_{S_{ik}} \varphi_{i_r}\mathcal{Q}_{ik}\left(\hat{\vec{v}}_i + \hat{\vec{v}}_k\right)dS,\end{aligned} \tag{A4}$$

where N_i represents the adjacent elements to the *i*-element and S_{ik} is the face between the *i*- and *k*-element. The matrices $\mathcal{P}_{ik}$ and $\mathcal{Q}_{ik}$ are defined as follows

$$\begin{aligned}\mathcal{P}_{ik} &= \sum_{\theta\in\{x,y,z\}} n_{ik_\theta}\mathcal{M}_\theta \\ \mathcal{Q}_{ik} &= \sum_{\theta\in\{x,y,z\}} n_{ik_\theta}\mathcal{N}_\theta\end{aligned}$$

where $n_{ik\theta}$ is the component along the θ axis of the unit normal vector $\vec{n}_{ik}$ of the face S_{ik} which points from the *i*- to the *k*-element.

[74] The local nature of DG-FEM is illustrated in (A4) through the surface integrals that only require the faces shared with the neighbor elements. Because the orthogonality of the residual must be accomplished with the complete space of test functions and using the tensor product $\otimes$, we obtain the expression

$$\begin{aligned}\rho_i(\mathcal{I}_3\otimes\mathcal{K}_i)\partial_t\vec{v}_i &= -\sum_{\theta\in\{x,y,z\}} (\mathcal{M}_\theta\otimes\mathcal{E}_{i\theta})\vec{\sigma}_i \\ &\quad + \frac{1}{2}\sum_{k\in N_i}[(\mathcal{P}_{ik}\otimes\mathcal{F}_{ik})\vec{\sigma}_i + (\mathcal{P}_{ik}\otimes\mathcal{G}_{ik})\vec{\sigma}_k] \\ (\Lambda_i\otimes\mathcal{K}_i)\partial_t\vec{\sigma}_i &= -\sum_{\theta\in\{x,y,z\}} (\mathcal{N}_\theta\otimes\mathcal{E}_{i\theta})\vec{v}_i \\ &\quad + \frac{1}{2}\sum_{k\in N_i}[(\mathcal{P}_{ik}\otimes\mathcal{F}_{ik})\vec{v}_i + (\mathcal{P}_{ik}\otimes\mathcal{G}_{ik})\vec{v}_k],\end{aligned} \tag{A5}$$

where $\mathcal{I}_3$ represents the identity matrix. In system (A5), the vectors $\vec{v}_i$ and $\vec{\sigma}_i$ should be read as the collection of all nodal values of the velocity and stress components in the *i*-element, respectively. The matrices involved in (A5) are: the mass matrix

$$(\mathcal{K}_i)_{rj} = \int_{V_i} \varphi_{i_r}\varphi_{i_j}dV \quad j,r \in [1,d_i],$$

the stiffness matrix

$$(\mathcal{E}_{i\theta})_{rj} = \int_{V_i} (\partial_\theta\varphi_{i_r})\varphi_{i_j}dV \quad j,r \in [1,d_i] \quad \theta \in \{x,y,z\},$$

and the flux matrices

$$(\mathcal{F}_{ik})_{rj} = \int_{S_{ik}} \varphi_{i_r} \varphi_{i_j} dS \quad j, r \in [1, d_i],$$

$$(\mathcal{G}_{ik})_{rj} = \int_{S_{ik}} \varphi_{i_r} \varphi_{i_j} dS \quad r \in [1, d_i] \quad j \in [1, d_k].$$

The scheme (A5) allows different approximation orders between adjacent elements, (i.e., p-adaptivity), and mesh refinement, (i.e., h-adaptivity). For more details see *Etienne et al.* [2010].

[75] This method was selected to implement the dynamic rupture because it is suitable for handling discontinuities across the elements boundaries through the application of *ad hoc* fluxes. Besides, the implementation of the DGCrack method into the GeoDG3D code (developed by *Etienne et al.* [2010]) was straightforward since we only need to recognize the fault surface in the domain and substitute the centered scheme fluxes with the *ad hoc* expressions derived in sections 3.2.1 and 3.2.2 over the fault, while leaving intact the rest of the code.

Appendix B: Matrices Used in the DG-FEM Formulation

[76] The following matrices are used in the DGCrack method and where previously introduced by *Benjemaa et al.* [2009].

[77] Matrices $\mathcal{M}_\theta$ and $\mathcal{N}_\theta$, required for the wave propagation scheme explained in the Appendix A, are constant real matrices defined as

$$\mathcal{M}_x = \begin{pmatrix} 1 & 1 & 0 & 0 & 0 & 0 \\ 0 & 0 & 0 & 1 & 0 & 0 \\ 0 & 0 & 0 & 0 & 1 & 0 \end{pmatrix} \quad \mathcal{N}_x = \begin{pmatrix} 1 & 2 & -1 & 0 & 0 & 0 \\ 0 & 0 & 0 & 1 & 0 & 0 \\ 0 & 0 & 0 & 0 & 1 & 0 \end{pmatrix}^T$$

$$\mathcal{M}_y = \begin{pmatrix} 0 & 0 & 0 & 1 & 0 & 0 \\ 1 & 0 & 1 & 0 & 0 & 0 \\ 0 & 0 & 0 & 0 & 0 & 1 \end{pmatrix} \quad \mathcal{N}_y = \begin{pmatrix} 0 & 0 & 0 & 1 & 0 & 0 \\ 1 & -1 & 2 & 0 & 0 & 0 \\ 0 & 0 & 0 & 0 & 0 & 1 \end{pmatrix}^T$$

$$\mathcal{M}_z = \begin{pmatrix} 0 & 0 & 0 & 0 & 1 & 0 \\ 0 & 0 & 0 & 0 & 0 & 1 \\ 1 & -1 & -1 & 0 & 0 & 0 \end{pmatrix} \quad \mathcal{N}_z = \begin{pmatrix} 0 & 0 & 0 & 0 & 1 & 0 \\ 0 & 0 & 0 & 0 & 0 & 1 \\ 1 & -1 & -1 & 0 & 0 & 0 \end{pmatrix}^T.$$

Matrix $\mathcal{S}$, required for the dynamic rupture model explained in section 3.2, is a symmetric positive definite matrix given by

$$\mathcal{S} = \begin{pmatrix} 1 & 0 & 0 & 0 & 0 & 0 \\ 0 & \frac{2}{3} & \frac{1}{3} & 0 & 0 & 0 \\ 0 & \frac{1}{3} & \frac{2}{3} & 0 & 0 & 0 \\ 0 & 0 & 0 & 1 & 0 & 0 \\ 0 & 0 & 0 & 0 & 1 & 0 \\ 0 & 0 & 0 & 0 & 0 & 1 \end{pmatrix}.$$

[78] **Acknowledgments.** We especially thank Steven Day for his advice and clarifications regarding some physical model considerations, for corrections of this manuscript, as well as for the cohesive zone resolution data of TPV3. We thank Christian Pelties for fruitful discussions and for providing us the TPV3 solutions by the ADER-DG and MDSBI codes. We thank Ana Rocher for drawing Figure 1. We thank Mondher Benjemaa for his comments and experience. Without the Gmsh software this work could not be possible, so we are grateful to its developers. We thank Alfonso Trejo, from HPC-Team, for his outstanding assistance in setting the parallel supercomputer Pohualli, in which all simulations were performed. We also thank Carl Gable for his advice on meshing strategies for the Landers earthquake fault-system. MDSBI solutions have been computed by Gilbert B. Brietzke. Finally, we thank David Oglesby and Jeremy Kozdon for their remarks and suggestions. This work has been possible thanks to the Mexican Consejo Nacional de Ciencia y Tecnología (CONACyT) under the grant number 80205, and partially supported by both the French Agence Nationale de la Recherche under the grant ANR-2011-BS56-017 and the European Marie Curie Actions-International Research Staff Exchange Scheme under the grant 295217.

References

Adda-Bedia, M., and R. Madariaga (2008), Seismic radiation from a kink on an antiplane fault, *Bull. Seismol. Soc. Am.*, *98*(5), 2291–2302, doi:10.1785/0120080003.

Ampuero, J. P. (2002), Etude physique et numérique de la nucléation des séismes, PhD thesis, Université Paris VII, Paris.

Andrews, D. J. (1976), Rupture velocity of plane strain shear cracks, *J. Geophys. Res.*, *81*(32), 5679–5687, doi:10.1029/JB081i032p05679.

Andrews, D. J. (1985), Dynamic plane-strain shear rupture with a slip-weakening friction law calculated by a boundary integral method, *Bull. Seismol. Soc. Am.*, *75*, 1–21.

Aochi, H., and E. Fukuyama (2002), Three-dimensional nonplanar simulation of the 1992 Landers earthquake, *J. Geophys. Res.*, *107*(B2), 2035, doi:10.1029/2000JB000061.

Aochi, H., E. Fukuyama, and M. Matsu'ura (2000), Spontaneous rupture propagation on a non-planar fault in 3-D elastic medium, *Pure Appl. Geophys.*, *157*(11–12), 2003–2027, doi:10.1007/PL00001072.

Aochi, H., R. Madariaga, and E. Fukuyama (2003), Constraint of fault parameters inferred from nonplanar fault modeling, *Geochem. Geophys. Geosyst.*, *4*(2), 1020, doi:10.1029/2001GC000207.

Barall, M. (2009), A grid-doubling finite-element technique for calculating dynamic three-dimensional spontaneous rupture on an earthquake fault, *Geophys. J. Int.*, *178*, 845–859, doi:10.1111/j.1365?246X.2009.04190.x.

Benjemaa, M., N. Glinsky, V. M. Cruz-Atienza, J. Virieux, and S. Piperno (2007), Dynamic non-planar crack rupture by a finite-volume method, *Geophys. J. Int.*, *171*, 271–285, doi:10.1111/j.1365-246X.2006.03500.x.

Benjemaa, M., N. Glinsky-Olivier, V. M. Cruz-Atienza, and J. Virieux (2009), 3-D dynamic rupture simulations by a finite volume method, *Geophys. J. Int.*, *178*(1), 541–560, doi:10.1111/j.1365-246X.2009.04088.x.

Brossier, R., S. Operto, and J. Virieux (2009), Seismic imaging of complex onshore structures by 2D elastic frequency-domain full-waveform inversion, *Geophysics*, *74*(6), 105–118, doi:10.1190/1.3215771.

Campillo, M., and R. Archuleta (1993), A rupture model for the 28 June 1992 Landers, California, earthquake, *Geophys. Res. Lett.*, *20*(8), 647–650, doi:10.1029/92GL02822.

Cianetti, S., C. Giunchi, and M. Cocco (2005), Three-dimensional finite element modeling of stress interaction: An application to Landers and Hector Mine fault systems, *J. Geophys. Res.*, *110*, B05S17, doi:10.1029/2004JB003384.

Cochard, A., and R. Madariaga (1994), Dynamic faulting under rate-dependent friction, *Pure Appl. Geophys.*, *142*, 419–445.

Cruz-Atienza, V. M. (2006), Rupture dynamique des faille non-planaires en différences finies, PhD thesis, Université Nice-Sophia Antipolis, Nice, France.

Cruz-Atienza, V. M., and K. B. Olsen (2010), Super shear mach-waves expose the fault breakdown slip, *Tectonophysics*, *493*, 285–296, doi:10.1016/j.tecto. 2010.05.012.

Cruz-Atienza, V. M., and J. Virieux (2004), Dynamic rupture simulation of non-planar faults with a finite-difference approach, *Geophys. J. Int.*, *158*, 939–954, doi:10.1111/j.1365?246X.2004.02291.x.

Cruz-Atienza, V. M., J. Virieux, and H. Aochi (2007), 3D finite-difference dynamic-rupture modeling along non-planar faults, *Geophysics*, *72*, SM123, doi:10.1190/1.2766756.

Cruz-Atienza, V. M., K. B. Olsen, and L. A. Dalguer (2009), Estimation of the breakdown slip from strong-motion seismograms: Insights from numerical experiments, *Bull. Seismol. Soc. Am.*, *99*(6), 3454–3469, doi:10.1785/0120080330.

Dalguer, L. A., and S. M. Day (2007), Staggered-grid split-node method for spontaneous rupture simulation, *J. Geophys. Res.*, *112*, B02302, doi:10.1029/2006JB004467.

Das, S., and K. Aki (1977), Fault plane with barriers: A versatile earthquake model, *J. Geophys. Res.*, *82*, 5658–5670.

Day, S. M. (1982), Three-dimensional simulation of spontaneous rupture: The effect of nonuniform prestress, *Bull. Seismol. Soc. Am.*, *72*(6), 1881–1902.

Day, S. M., L. A. Dalguer, N. Lapusta, and Y. Liu (2005), Comparison of finite difference and boundary integral solutions to three-dimensional spontaneous rupture, *J. Geophys. Res.*, *110*, B12307, doi:10.1029/2005JB003813.

de la Puente, J., J. P. Ampuero, and M. Käser (2009), Dynamic rupture modeling on unstructured meshes using a discontinuous galerkin method, *J. Geophys. Res.*, *114*, B10302, doi:10.1029/2008JB006271.

Delcourte, S., L. Fezoui, and N. Glinsky-Olivier (2009), A high-order discontinuous Galerkin method for the seismic wave propagation, *ESAIM Proc.*, *27*, 70–89.

Dieterich, J. (1979), Modeling of rock friction: 1. Experimental results and constitutive equations, *J. Geophys. Res.*, *84*(B5), 2161–2168, doi:10.1029/JB084iB05p02161.

Duan, B., and S. M. Day (2008), Inelastic strain distribution and seismic radiation from rupture of a fault kink, *J. Geophys. Res.*, *113*, B12311, doi:10.1029/2008JB005847.

Dumbser, M., and M. Käser (2006), An arbitrary high-order discontinuous Galerkin method for elastic waves on unstructured meshes II: The three-dimensional isotropic case, *Geophys. J. Int.*, *167*(1), 319–336.

Ely, G., S. M. Day, and J. B. Minster (2009), A support-operator method for 3D rupture dynamics, *Geophys. J. Int.*, *177*, 1140–1150, doi:10.1111/j.1365-246X.2009.04117.x.

Etienne, V., E. Chaljub, J. Virieux, and N. Glinsky (2010), An hp-adaptive discontinuous Galerkin finite-element method for 3-D elastic wave modelling, *Geophys. J. Int.*, *183*(2), 941–962, doi:10.1111/j.1365-246X.2010.04764.x.

Festa, G., and J. P. Vilotte (2006), Influence of the rupture initiation on the intersonic transition: Crack-like versus pulse-like modes, *Geophys. Res. Lett.*, *33*, L15320, doi:10.1029/2006GL026378.

Fialko, Y. (2004), Probing the mechanical properties of seismically active crust with space geodesy: Study of the coseismic deformation due to the 1992 Mw 7.3 Landers (southern California) earthquake, *J. Geophys. Res.*, *109*, B03307, doi:10.1029/2003JB002756.

Geubelle, P., and J. Rice (1995), A spectral method for threedimensional elastodynamic fracture problems, *J. Mech. Phys. Solids*, *43*, 1791–1824.

Geuzaine, C., and J. F. Remacle (2009), Gmsh: A three-dimensional finite element mesh generator with built-in pre- and post-processing facilities, *Int. J. Numer. Methods Eng.*, *79*(11), 1309–1331.

González-Casanova, P. (2006), Solución numérica de leyes de conservación hiperbólicas, in *Notas de Modelación y Métodos Numéricos I.* CIMAT y CIMNE., Guanajuato, México.

Guatteri, M., and P. Spudich (2000), What can strong-motion data tell us about slip-weakening fault-friction laws?, *Bull. Seismol. Soc. Am.*, *90*(1), 98–116, doi:10.1785/0119990053.

Harris, R. A., and S. M. Day (1993), Dynamics of fault interaction: Parallel strike-slip faults, *J. Geophys. Res.*, *98*(B3), 4461–4472.

Harris, R. A., et al. (2009), The SCEC/USGS dynamic earthquake-rupture code verification exercise, *Seismol. Res. Lett.*, *80*(1), 119–126, doi:10.1785/gssrl.80.1.119.

Hernández, B., F. Cotton, and M. Campillo (1999), Contribution of radar interferometry to a two-step inversion of kinematic process of the 1992 Landers earthquake, *J. Geophys. Res.*, *104*(B6), 13,083–13,099, doi:10.1029/1999JB900078.

Hesthaven, J. S., and T. Warburton (2008), *Nodal Discontinuous Galerkin Methods: Algorithms, Analysis and Applications*, 1st ed., 515 pp., Springer, New York.

Hok, S., and E. Fukuyama (2011), A new BIEM for rupture dynamics in half-space and its application to the 2008 Iwate-Miyagi Nairiku earthquake, *Geophys. J. Int.*, *184*, 301–324, doi:10.1111/j.1365-246X.2010.04835.x.

Ida, Y. (1972), Cohesive force across the tip of a longitudinal-shear crack and Griffith's specific surface energy, *J. Geophys. Res.*, *77*, 3796–3805.

Ide, S., and M. Takeo (1997), Determination of constitutive relations of fault slip based on seismic wave analysis, *J. Geophys. Res.*, *102*(B12), 27,379–27,391, doi:10.1029/97JB02675.

Kame, N., and T. Yamashita (1999), Simulation of the spontaneous growth of a dynamic crack without constraints on the crack tip path, *Geophys. J. Int.*, *139*(2), 345–358, doi:10.1046/j.1365-246x.1999.00940.x.

Kaneko, Y., N. Lapusta, and J. P. Ampuero (2008), Spectral element modeling of spontaneous earthquake rupture on rate and state faults: Effect of velocity-strengthening friction at shallow depths, *J. Geophys. Res.*, *113*, B09317, doi:10.1029/2007JB005553.

Kase, Y., and S. M. Day (2006), Rupture processes on a bending fault, *Geophys. Res. Lett.*, *33*, L10601, doi:10.1029/2006GL025865.

Käser, M., and M. Dumbser (2008), A highly accurate discontinuous Galerkin method for complex interfaces between solids and moving fluids, *Geophysics*, *73*(3), 23–35.

Knopoff, L., and X. X. Ni (2001), Numerical instability at the edge of a dynamic fracture, *Geophys. J. Int.*, *147*(3), 1–6, doi:10.1046/j.1365-246x.2001.01567.x.

Kozdon, J. E., E. M. Dunham, and J. Nordstrom (2012), Simulation of dynamic earthquake ruptures in complex geometries using high-order finite difference methods, *J. Sci. Comput.*, doi:10.1007/s10915-012-9624-5, in press.

Lapusta, N., J. R. Rice, Y. Ben-Zion, and G. Zheng (2000), Elastodynamic analysis for slow tectonic loading with spontaneous rupture episodes on faults with rate- and state-dependent friction, *J. Geophys. Res.*, *105*(23), 765–790.

Levander, A. R. (1988), Fourth-order finite-difference P-SV seismograms, *Geophysics*, *53*(11), 1425–1436.

LeVeque, R. J. (2002), *Finite Volume Methods for Hyperbolic Problems*, 1st ed., 578 pp., Cambridge Univ. Press, Cambridge, U. K.

Ma, S., and R. J. Archuleta (2006), Radiated seismic energy based on dynamic rupture models of faulting, *J. Geophys. Res.*, *111*, B05315, doi:10.1029/2005JB004055.

Madariaga, R. (1976), Dynamics of an expanding circular fault, *Bull. Seismol. Soc. Am.*, *66*(3), 5679–5687.

Madariaga, R., K. Olsen, and R. Archuleta (1998), Modeling dynamic rupture in a 3D earthquake fault model, *Bull. Seismol. Soc. Am.*, *88*(5), 1182–1197.

Mikumo, T., and Y. Yagi (2003), Slip-weakening distance in dynamic rupture of in-slab normal-faulting earthquakes, *Geophys. J. Int.*, *155*(2), 443–455.

Miyatake, T. (1980), Numerical simulations of earthquake source process by a three-dimensional crack model. Part I rupture process, *J. Phys. Earth*, *28*(6), 565–598.

Moczo, P., J. Kristek, M. Galis, P. Pazak, and M. Balazovjech (2007), The finite-difference and finite-element modeling of seismic wave propagation and earthquake motion, *Acta Phys. Slovaca*, *57*(2), 177–406.

Nielsen, S. B. (1998), Free surface effects on the propagation of dynamic rupture, *Geophys. Res. Lett.*, *25*(1), 125–128, doi:10.1029/97GL03445.

Oglesby, D. D., and S. M. Day (2001), The effect of fault geometry on the 1999 Chi-Chi (Taiwan) earthquake, *Geophys. Res. Lett.*, *28*, 1831–1834.

Oglesby, D. D., R. J. Archuleta, and S. B. Nielsen (1998), Earthquakes on Dipping Faults: The Effects of Broken Symmetry, *Science*, *280*(5366), 1055–1059, doi:10.1126/science.280.5366.1055.

Olsen, K. B., R. Madariaga, and R. J. Archuleta (1997), Three-dimensional dynamic simulation of the 1992 Landers earthquake, *Science*, *278*(5339), 834–838, doi:10.1126/science.278.5339.834.

Palmer, A., and J. R. Rice (1973), The grow of slip surfaces in the progressive failure of over-consolidated clay, *Proc. R. Soc. A*, *332*, 527–548.

Pelties, C., J. de la Puente, J. Ampuero, G. Brietzke, and M. Käser (2012), Three-dimensional dynamic rupture simulation with a high-order Discontinuous Galerkin method on unstructured tetrahedral meshes, *J. Geophys. Res.*, *117*, B02309, doi:10.1029/2011JB008857.

Peyrat, S., K. B. Olsen, and R. Madariaga (2001), Dynamic modeling of the 1992 Landers earthquake, *J. Geophys. Res.*, *106*(26), 467–482.

Plesch, A., et al. (2007), Community Fault Model (CFM) for Southern California, *Bull. Seismol. Soc. Am.*, *97*(6), 1793–1802, doi:10.1785/0120050211.

Remaki, L., O. Hassan, and K. Morgan (2011), Aerodynamic computations using a finite volume method with an HLLC numerical flux function, *Math. Modell. Nat. Phenom.*, *6*(3), 189–212.

Remaki, M. (2000), A new finite volume scheme for solving Maxwell's system, *Int. J. Comput. Math. Electr. Electr. Eng.*, *19*(3), 913–931.

Rojas, O., E. Dunham, S. M. Day, L. A. Dalguer, and J. E. Castillo (2009), Finite difference modeling of rupture propagation with strong velocity-weakening friction, *Geophys. J. Int.*, *179*, 1831–1858, doi:10.1111/j.1365-246X.2009.04387.x.

Ruina, A. (1983), Slip instability and state variable friction laws, *J. Geophys. Res.*, *88*(B12), 10,359–10,370, doi:10.1029/JB088iB12p10359.

Spudich, P., and M. Guatteri (2004), The effect of bandwidth limitations on the inference of earthquake slip-weakening distance from seismograms, *Bull. Seismol. Soc. Am.*, *94*(6), 2028–2036, doi:10.1785/0120030104.

Tago, J., V. M. Cruz-Atienza, V. Etienne, J. Virieux, E. Chaljub, M. Benjemaa, and F. J. Sánchez-Sesma (2010), 3-D dynamic rupture with anelastic wave propagation using an hp-adaptive discontinuous galerkin method, Abstract S51A-1915 presented at 2010 Fall Meeting, AGU, San Francisco, Calif., 13-17 Dec.

Virieux, J., and R. Madariaga (1982), Dynamic faulting studied by a finite difference method, *Bull. Seismol. Soc. Am.*, *72*(2), 345–369.

Wald, D., and T. Heaton (1994), Spatial and temporal distribution of slip for the 1992 Landers, California, earthquake, *Bull. Seismol. Soc. Am.*, *84*(3), 668–691.

Zienkiewicz, O. C., R. L. Taylor, and J. Z. Zhu (2005), *Finite Element Method: Its Basis and Fundamentals*, 6th ed., 752 pp., Butterworth-Heinemann, Oxford, U. K.